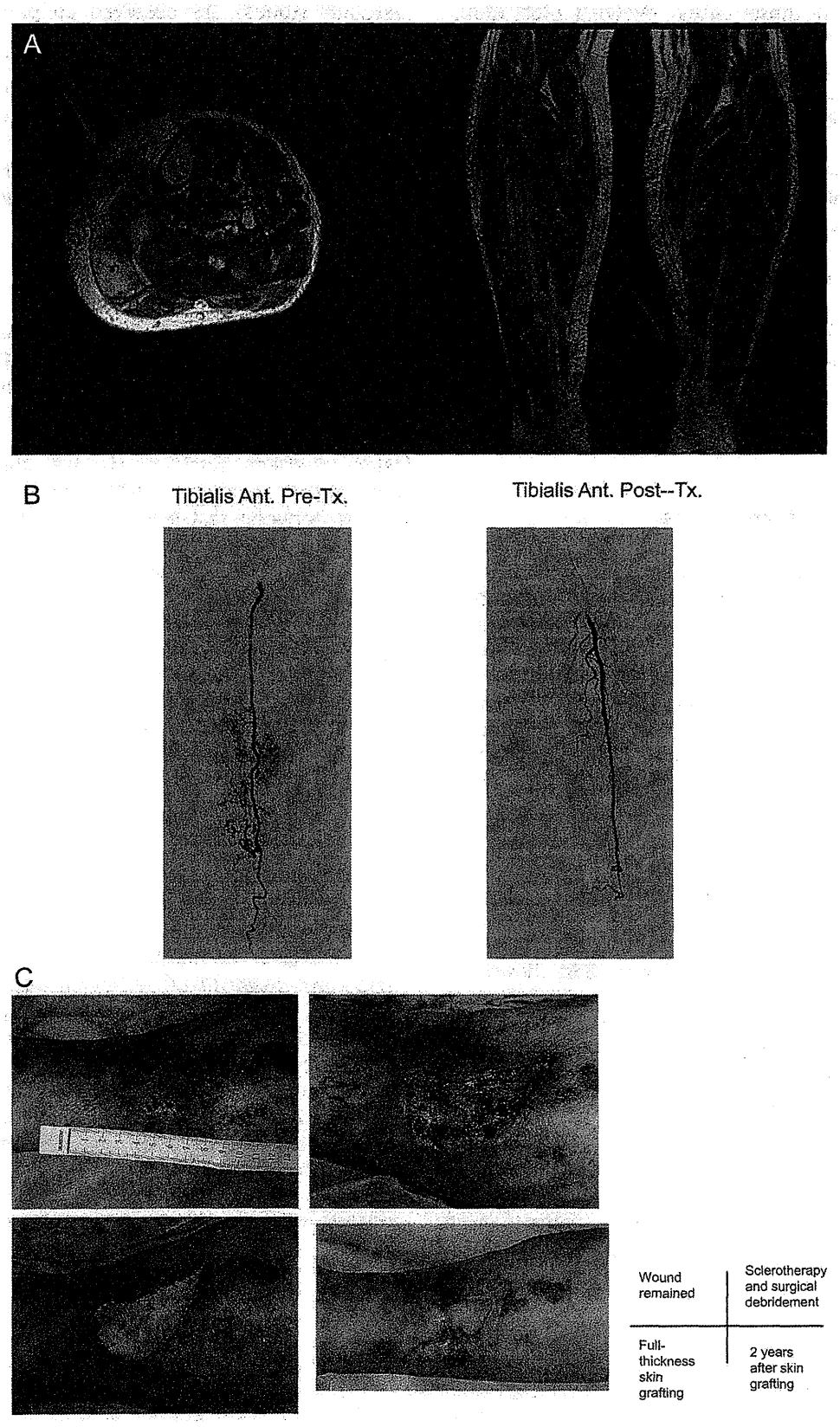
A
B
Tibialis Ant. Pre-Tx.
Tibialis Ant. Post--Tx.
C
Wound remained
Sclerotherapy and surgical debridement
Full-thickness skin grafting
2 years after skin grafting

MRI

MRI is the best diagnostic technique, providing optimal analysis of soft-tissue masses and accurate diagnosis, and can be used to distinguish tissular form cystic lesions, and delineate fast or slow vessel flows. Venous and lymphatic malformations may demonstrate a similar pattern. They are hyperintense on spin-echo T2-weighed sequences and optimally seen in fat-suppression sequences. T1-weighed and fat-suppression sequences with gadolinium injection demonstrate intense enhancement in IH, whereas enhancement is inconsistent and progressive on dynamic sequences in VMs. Gadolinium contrast medium enables differential diagnosis among VMs and LMs. LMs can be distinguished from VMs, as LMs indicate enhancement only at the margins of cysts. By contrast, VMs enhance clearly and homogeneously. MRI is essential before treatment to determine the extent of the lesion and the relationship between the vascular malformation and intact neighbouring nerves and vessels. It is also useful for identification and diagnosis of the lesion. In fast-flow vessels, they are identified as flow voids.

Magnetic resonance angiography (MRA) can confirm the diagnosis of fast-flow vessels; however, it remains insufficient to accurately depict the nidus of AVMs and for analysis of angiostructures.

Vascular imaging

Vascular imaging is used mainly for fast-flow vascular lesions. Angiography is a superior pretreatment assessment of AVMs, which have characteristic early venous drainage. The angiostructure of an AVM can be obtained by identifying its location, arterial supplying vessels, draining veins, and the relationship with normal neighbouring arteries and veins. Angiography is used for diagnosis of quiescent AVMs, which simulate capillary malformation.

Clinical course and treatment

IH

Typically, IH involutes within a year or so. However, skin sequelae may exhibit telangiectasia, anetoderma (shrink skin), and fibro-fatty residual tissue (Fig. 1). When the lesion is beneath clothing, there is no functional loss or damage, and no further treatment but observation is required, careful and regular check-ups are advised. IHs may occasionally demonstrate ulceration in the plateau (22%) and involution (13%) phases, although this typically occurs during the proliferating phase [3]. Once finally involuted and regressed, if the IH lesion occupies a functional vital organ or is in an aesthetically important exposed area, surgery should be attempted to reconstruct and reduce the size. When the lesion is located in the eye, the visual acuity may be disturbed and the visual field may be limited. In cases such as these, surgical removal of the involuted and regressed skin in the upper eye and removal of the cheek tissue toward the lateral side is indicated (Fig. 2).

Atypical haemangioma

Some congenital haemangiomas, distinctive of IH, demonstrate a unique clinical course without spontaneous reduction in size even after 4 years (Fig. 3). This predominately occurs with NICH in which findings at duplex Doppler and ultrasound often depict arteriovenous shunting (Fig. 4).

VM

VMs are volume-occupying lesions containing abnormal and enlarged veins [7]. Although the lesion rarely develops an ulcer, a secondary ulcer and subsequent haemorrhage may develop due to the mass and higher pressure on tissues adjacent to the sharp, hard tissue. This occurs principally in lesions located in the oral cavity, tongue, and lip, whereby teeth can lacerate the vermillion border of the lip, with consequent pain and swelling (Fig. 5A, arrow). Serial sclerotherapy can be performed to reduce the volume of the lesion and control the abnormal blood pooling and communication with the surrounding tissues. Better functional and aesthetic outcome can be obtained after removal of excessive tissue and reconstruction (Fig. 5).

Figure 6 A 73-year-old woman with an AVM in the right medial and lateral lower calf. A: Preoperative T2-weighed MRI image. Arrows indicate the nidus due to the AVM. B: Angiogram in the tibialis anterior demonstrated the fast flow and subsequent early entry in the venous drain, indicating the AVMs (left) and after embolization using NBCA to control flow supply and drainage (right). C: Within 24 h after embolization, percutaneous ultrasonic-guided sclerotherapy followed by surgical debridement and skin grafting. The wound remained healed at 2 years.

AVMs

AVMs are the most frequently occurring skin lesion among the vascular malformations. AVM can develop into ulcers during the natural clinical course and as a result of post-therapeutic morbidity from embolization or sclerotherapy, as the blood flow and perfusion in the local tissues are erroneous and unpredictable with [8] or without pre-existing disease [9]. Embolization using N-butyl cyanoacrylate (NBCA) can be used to control flow supply and drainage, and subsequent percutaneous or transcutaneous ultrasonic-guided sclerotherapy within 24 h may generate sufficient reconstruction of the wound bed. Additional sclerotherapy is used to suppress and control vessel malformations that are tiny or invisible at angiography. Surgical debridement and reconstruction are then performed (Fig. 6).

Treatment

Some vascular tumours (haemangiomas) and vascular malformations develop wounds and ulcers. Medication and management will follow clinical and imaging diagnostics. AVMs generally demonstrate the most severe ulcers, but ulcerated IH may produce intractable pain in the perioral region. Topical use of a sealant and systemic corticosteroid may control the pain, with easy access to feeding and healing of the ulcer itself [10]. Corticoids may induce cessation of the patient's growth if used other than during the growing phase of IH [11]. Thus, other agents, such as β-blockers, have recently been used for periods of 2–6 weeks and exhibit earlier wound healing and regression of the tumour [12].

By contrast, in the chronic stasis ulcer, arteriovenous communication resembling the features of AVMs causes rapid-growth ulceration [8]. Skin necrosis is demonstrated on the hands in patients with primary AVM ulcers as well as in 40% of patients after treatment with embolo/sclerotherapy [9].

In AVMs, a practical clinical staging system is proposed, which describes the progression of AVMs proposed by Schobinger [13]. In the initial quiescent stage (stage I), the lesion presents as warm, pink–blue macules. It subsequently expands with pulsations, thrills, and bruits (stage II), and eventually becomes destructive with pain, haemorrhage, or ulceration (stage III). The final stage demonstrates decompensation and results in congestive heart failure (stage IV) [13]. Ideally treatment should commence at stages I and II, but frequently, AVMs will not be detected until stage III, when ulceration is observed as a destructive clinical sign. In the study of Kohout et al., with a mean follow-up of 4.6 years, the cure rate of AVMs was reported as 75% for stage I, 67% for stage II, and 48% for stage III [13]. AVMs are exacerbated after trauma, hormonal change, pregnancy, or puberty. Duplex ultrasonic and clinical signs and symptoms can assist in therapeutic decision-making; however, more precise and effective evaluation using MRI and angiography are necessary. Although MRI can provide insight into the spatial relationship between the lesion and the surrounding tissues and organs, angiography is most important for the assessment of abnormal vasculature and therapeutic evaluation when embolization is required. Embolization is most often necessary for the abolition or reduction of the nidus, which denotes the main lesion of vascular shunting, supplying flow, pooling, and drainage. When AVM lesions are localized, as often seen in stage II, and are distinct from vital organs, either surgical removal alone or combined therapy with precedent embolization within 24–48 h is the initial choice of treatment. If the defect is large, reconstruction will follow [14]. If the lesion is extensive or destructive (stage III) and the lesion is not clearly delineated, controlled attenuation of the lesion should be considered.

Conclusion

The treatment of wounds caused by vascular anomalies involves detailed assessment of the clinical manifestations and imaging data. Control of the pathological abnormal vasculature precedes surgical removal and reconstruction. In vascular tumours, clinical diagnosis and observation are important, whereas extensive imaging is useful in vascular malformations, especially in AVMs.

Conflict of interest

The authors do not hold any conflict of interest in the content of this manuscript.

References

[1] Enjolras O, Mulliken JB. Vascular tumors and vascular malformations. Adv Dermatol 1997;13:375–423.
[2] Wassef M, Enjolrad O. Superficial vascular malformations: classification and histopathology. Ann Pathol 1999;19: 253–64.
[3] Chamlin SL, Haggstrom AN, Drolet BA, Baselga E, Frieden IJ, Garzon MC, et al. Multicenter prospective study of ulcerated hemangiomas. J Pediatr 2007;151:684–9.

[4] Maguiness SM, Hoffman WY, McCalmont TH, Frieden IJ. Early white discoloration of infantile hemangioma: a sign of impending ulceration. Arch Dermatol 2010;146:1235–9.
[5] Cavalli R, Buffon RB, de Souza M, Colli AM, Gelmetti C. Tumor lysis syndrome after propranolol therapy in ulcerative infantile hemangioma: rare complication or incidental finding? Dermatology 2012;224:106–9.
[6] Paltiel HJ, Burrows PE, Kozakewich HP, Zurakowski D, Mulliken JB. Soft tissue vascular anomalies: utility of US for diagnosis. Radiology 2000;214:747–54.
[7] Berenguer B, Burrows PE, Zurakowski D, Mulliken JB. Sclerotherapy of craniofacial venous malformations: complication and results. Plast Reconstr Surg 1999;104:1–11.
[8] Komai H, Kawago M, Juri M. Massive spouting bleeding from chronic stasis ulceration caused by arteriovenous communication of the lower extremity. J Vasc Surg 2006;44:658–9.
[9] Park UJ, Do YS, Park KB, Park HS, Kim YW, Lee BB, et al. Treatment of arteriovenous malformations involving the hand. Ann Vasc Surg 2012;26:643–8.
[10] Strand M, Smidt AC. Pain management for ulcerated infantile hemangiomas. Pediatr Dermatol 2012;29:124–6.
[11] Akhavan A, Zippin JH. Current treatments for infantile hemangiomas. J Drugs Dermatol 2010;9:176–80.
[12] Kim LH, Hogeling M, Wargon O, Jiwane A, Adams S. Propranol: useful therapeutic agent for ulcerated infantile hemangiomas. J Pediatr Surg 2011;46:759–63.
[13] Kohout MP, Hansen M, Pribaz JJ, Mulliken JB. Arteriovenous malformations of the head and neck: natural history and management. Plast Reconstr Surg 1998;102:643–54.
[14] Marler JJ, Mulliken JB. Current management of hemangiomas and vascular management. Clin Plast Surg 2005;32: 99–116.

J Ped Surg Case Reports 1 (2013) 29–31

Contents lists available at SciVerse ScienceDirect

Journal of Pediatric Surgery CASE REPORTS

journal homepage: www.jpscasereports.com

Prenatally detected giant congenital hemangioma of the fetal neck

Shuichiro Uehara [a,b,*], Toshimichi Hasegawa [a], Hiroomi Okuyama [a], Hisayoshi Kawahara [a], Akio Kubota [a], Keigo Osuga [c], Eiichi Morii [d]

[a] Department of Pediatric Surgery, Osaka Medical Center and Research Institute for Maternal and Child Health, Osaka 594-1101, Japan
[b] Division of Pediatric Surgery, Department of Surgery, Osaka University Graduate School of Medicine, Osaka 565-0871, Japan
[c] Department of Diagnostic and Interventional Radiology, Osaka University Graduate School of Medicine, Osaka 565-0871, Japan
[d] Department of Pathology, Osaka University Graduate School of Medicine, Osaka 565-0871, Japan

ARTICLE INFO

Article history:
Received 16 February 2013
Received in revised form
1 March 2013
Accepted 1 March 2013

Key words:
Congenital hemangioma
Antenatally detected
Magnetic resonance imaging

ABSTRACT

Hemangiomas and vascular malformations constitute a variety of non-cancerous birthmarks and lesions. We experienced a rare case of a fetus with a giant congenital hemangioma detected on the fetal ultrasonography and magnetic resonance imaging (MRI). The patient was delivered via a planned cesarean section and underwent extirpation of the tumor on the 16th postnatal day due to concerns of bleeding from the tumor. A pathological examination demonstrated glucose transporter (GLUT)-1-negative lobular capillary proliferation compatible with a diagnosis of congenital hemangioma. The infant was discharged without complications on day 14 after tumor resection. Currently, at 5 years of age, no tumor recurrence has so far been observed since the extirpation. The antenatal images of this case are presented and the perinatal management is discussed.

Congenital hemangiomas (CHs) are fully formed at birth, having undergone proliferation in utero, do not exhibit the typical postnatal evolutive pattern of infantile hemangioma (IH) and can be diagnosed prenatally using ultrasonography [1]. CH is a subtype of benign vascular tumor, that is further characterized as either rapidly involuting (RICH) or non-involuting (NICH). In most infants with RICH, involution is complete, leaving anetodermic skin within 6–14 months of life, whereas NICH lesions grow proportionally with the child's growth. NICHs never disappear and therefore require eventual excision. However, when CH is prenatally detected and there are concerns of bleeding or heart failure due to the high blood flow of the tumor, surgical resection may be performed immediately after birth.

We herein report a rare case of a fetus with a giant congenital hemangioma detected on the fetal ultrasonography and magnetic resonance imaging (MRI) that was treated with surgical resection.

1. Case report

A 29-year-old female was referred at 29 weeks of gestation due to an ultrasonographically detected tumor located on the fetal posterior neck. Ultrasonography revealed a 65 × 67 × 43-mm heterogeneous tumor that made contact with the infant's spine and skull (Fig. 1A). Color Doppler imaging revealed rich vascular formation and blood flow in the tumor. T2-weighted images of magnetic resonance imaging (MRI) obtained at 34 weeks of gestation revealed iso-high signal intensity (Fig. 1B). These findings were compatible with a diagnosis of hemangioma. During the pregnancy, fetal echography showed no increases tumor size; however, a mild right heart load was detected.

At 38 weeks of gestation, a planned cesarean section was performed with appropriate informed consent to prevent dystocia and bleeding from the tumor during vaginal delivery. A 2622-g-male infant was delivered with Apgar scores of 8 and 9 at one and 5 min, respectively. The infant did not require resuscitation or respiratory support. The tumor originated from the posterior of the neck, as observed on prenatal images. The color of the tumor became more red with each passing day, and the surface of the tumor gradually demonstrated enlargement, creating an ulcer on the surface of the tumor (Fig. 2). No signs of involution of the tumor were observed until the 15th postnatal day. Since the tumor appeared ready to bleed from the surface, tumor resection was performed on the 16th postnatal day. First, a spindle-shaped skin incision was made around the tumor. Tumor mobilization was achieved with fine ligations of the vessels in the subcutanous lesion, preserving the posterior neck muscles. The tumor was successfully resected completely. Skin grafting was not required to close the wound. The amount of blood loss was 132 ml, and the operative time was 3 h and 13 min. A pathological examination revealed lobular capillary

* Corresponding author. Division of Pediatric Surgery, Department of Surgery, Osaka University Graduate School of Medicine, 2-2 Yamadaoka, Suita, Osaka 565-0871, Japan. Tel.: +81 6 6879 3753; fax: +81 6 6879 3759.
E-mail address: uehara@pedsurg.med.osaka-u.ac.jp (S. Uehara).

2213-5766/$ – see front matter © 2013 Elsevier Inc. All rights reserved.
http://dx.doi.org/10.1016/j.epsc.2013.03.003

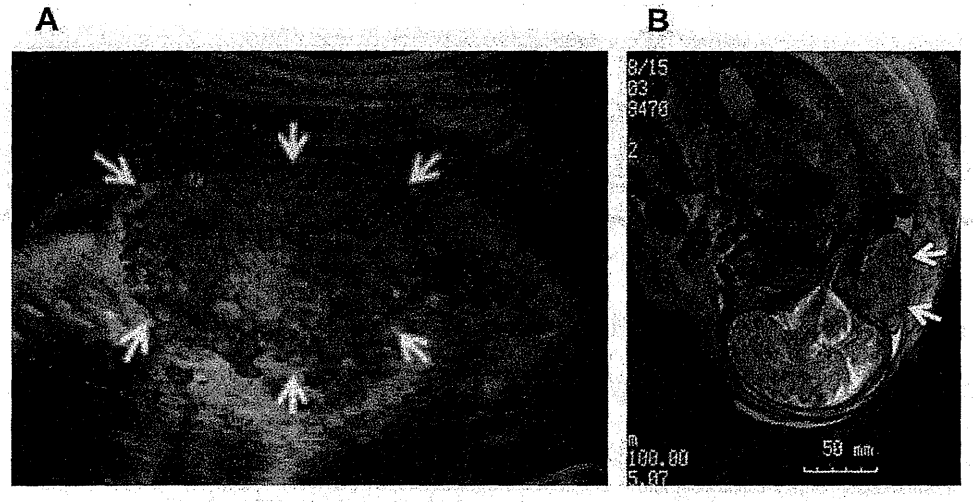

Fig. 1. Prenatal images of color Doppler ultrasonography at 29 weeks of gestation showing the 65 × 67 × 43-mm heterogeneous tumor that made contact with the infant's spine and skull. Rich vascular formation and blood flow in the tumor was observed (A). T2-weighted images of magnetic resonance imaging (MRI) obtained at 34 weeks of gestation revealed iso-high signal intensity (B).

proliferation (Fig. 3A) and a GLUT-1-negative status in the vascular endothelial cells, in contrast to the positive findings in red blood cells observed in the vessels as an internal control of GLUT-1 (Fig. 3B), compatible with a diagnosis of congenital hemangioma. The infant was discharged without complications on day 14 after tumor resection. Currently, at age 5 years of age, no tumor recurrence has not been observed since the tumor resection.

2. Discussion

The concept of a classification system for pediatric vascular anomalies was first established in 1982 based on the pathologic findings reported in a study by Mulliken and Glowacki and later modified by the International Society for the Study Group of Vascular Anomalies [2]. Congenital hemangioma (CH) is a subtype of benign vascular tumor that is further characterized as rapidly involuting (RICH) or non-involuting (NICH). Infantile hemangioma (IH) and CH are distinguished based on their clinical features and the presence of a GLUT-1-positive expression in the endothelial cells of infantile hemangioma (IH) [3]. The involution observed in cases of RICH is very similar to that observed in cases of IH, which regresses slowly after occurring during the first year of life [4]. In contrast, NICH does not exhibit the regression. Consequently, the possibility of NICH being a later stage of RICH has been suggested. Therefore, to determine the fate of RICH and NICH, monitoring for an observation period of a few years and performing serial postnatal imaging can provide insight into imaging evolution and involution of RICH during the first year of life.

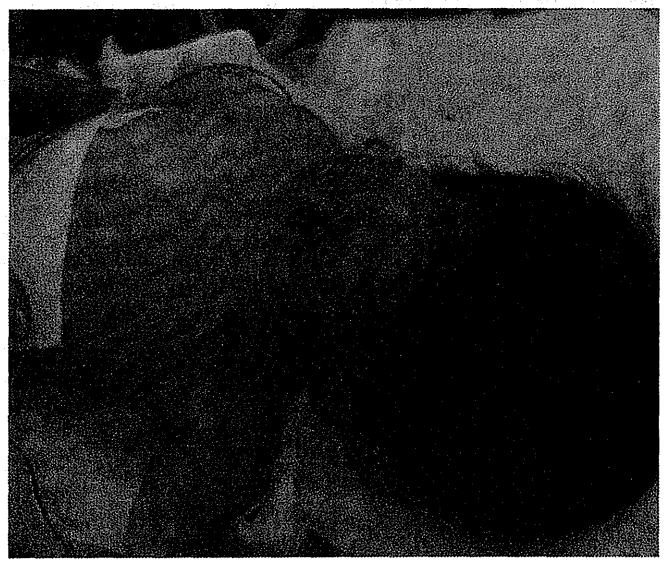

Fig. 2. Postnatal photograph showing the neonate with a tumor on the posterior neck.

Both CH and IH appear as fast-flow lesions on ultrasound and exhibit flow voids on MRI. RICH and NICH are more likely to be heterogeneous on US and much more likely to contain identifiable calcification. On MRI, these lesions exhibit high intensity on T2-weighted images and iso-intensity on T1-weighted images; prior to involution, they enhance avidly and homozygously [5]. Fast-flow is also detected in arterial vascular malformations; however, it can be easily differentiated on MRI. Prenatal screening with ultrasonography allows for the early detection of CH as early as 12 weeks of gestation [4]. A distinction between RICH and NICH lesions cannot be made on prenatal ultrasound [6]. If CH is diagnosed antenatally, the lesion can be followed on ultrasonography and MRI to further define the tumor characteristics and monitor growth [7].

In our case, immunohistochemical staining revealed negative GLUT-1 results, suggesting a diagnosis of CH. However, it is difficult to distinguish RICH from NICH before and at birth without the knowledge obtained from histological findings and observation for at least one year. Since the tumor in our case was likely to be injured by mechanical friction, we believed that it should be excised without observation to distinguish involution.

As Nolan et al. [8] previously reported, life-threatening hemorrhage associated with passage through the birth canal can result in by birth trauma if the tumor is large and located on the surface of the neonate. In such cases, cesarean section should be used for delivery. Bleeding may also occur, even after birth, due to mechanical friction. Powell et al. [9] reported that two cases of severe bleeding episodes occurred during the first week of life. Close antenatal evaluation, including the frequent use of US to monitor lesion size and blood flow, should be conducted. Large hemangiomas can cause congestive heart failure due to hyperdynamic circulation leading to increasing cardiac output; therefore, fetal circulatory parameters should also be monitored. When these findings are observed, surgical excision should be considered

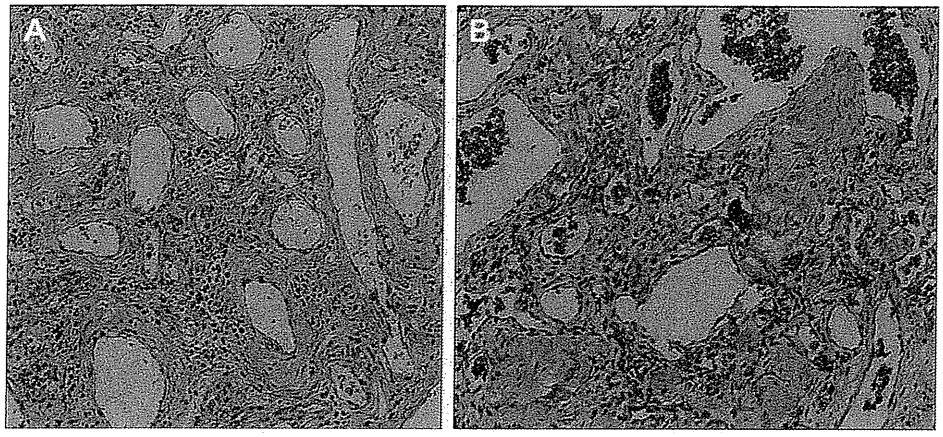

Fig. 3. Microscopic examination showing capillaries and feeding vessels with flattened endothelial cells on hematoxylin eosin staining (A, ×200). GLUT-1 immunostaining was negative (B, ×200), consistent with a diagnosis of congenital hemangioma.

immediately after birth. Otherwise, the first line of treatment should be close observation.

3. Conclusion

We herein reported a rare case of a fetus with a giant congenital hemangioma detected on the fetal ultrasonography and MRI that was treated with the extirpation. Close follow-up before and after birth led to concerns of bleeding after birth, and a surgical approach was ultimately selected.

Conflicts of interest

None.

Sources of funding

None.

Acknowledgement

The authors thank Dr. Brian Quinn, Japan Medical Communication for editing this manuscript.

References

[1] Brix M, Soupre V, Enjolras O, Vazquez MP. Antenatal diagnosis of rapidly involuting congenital hemangiomas (RICH). Rev Stomatol Chir Maxillofac 2007; 108:109–14.
[2] Mulliken JB, Enjolras O. Congenital hemangiomas and infantile hemangioma: missing links. J Am Acad Dermatol 2004;50:875–82.
[3] North PE, Waner M, Mizeracki A, Mrak RE, Nicholas R, Kincannon J, et al. A unique microvascular phenotype shared by juvenile hemangiomas and human placenta. Arch Dermatol 2001;137:559–70.
[4] Berenguer B, Mulliken JB, Enjolras O, Boon LM, Wassef M, Josset P, et al. Rapidly involuting congenital hemangioma: clinical and histopathologic features. Pediatr Dev Pathol 2003;6:495–510.
[5] Gorincour G, Kokta V, Rypens F, Garel L, Powell J, Dubois J. Imaging characteristics of two subtypes of congenital hemangiomas: rapidly involuting congenital hemangiomas and non-involuting congenital hemangiomas. Pediatr Radiol 2005;35:1178–85.
[6] Fadell 2nd MF, Jones BV, Adams DM. Prenatal diagnosis and postnatal follow-up of rapidly involuting congenital hemangioma (RICH). Pediatr Radiol 2011;41: 1057–60.
[7] Ozcan UA. Rapidly involuting congenital hemangioma: a case of complete prenatal involution. J Clin Ultrasound 2010;38:85–8.
[8] Nolan M, Hartin Jr CW, Pierre J, Ozgediz DE. Life-threatening hemorrhage from a congenital hemangioma caused by birth trauma. J Pediatr Surg 2012;47: 1016–8.
[9] Powell J, Blouin MM, David M, Dubois J. Bleeding in congenital hemangiomas: crusting as a clinical predictive sign and usefulness of tranexamic acid. Pediatr Dermatol 2012;29:182–5.

Apelin Inhibits Diet-Induced Obesity by Enhancing Lymphatic and Blood Vessel Integrity

Mika Sawane,[1,2] Kentaro Kajiya,[2] Hiroyasu Kidoya,[1] Masaya Takagi,[2] Fumitaka Muramatsu,[1] and Nobuyuki Takakura[1]

Angiogenesis is tightly associated with the outgrowth of adipose tissue, leading to obesity, which is a risk factor for type 2 diabetes and hypertension, mainly because expanding adipose tissue requires an increased nutrient supply from blood vessels. Therefore, induction of vessel abnormality by adipokines has been well-studied, whereas how altered vascular function promotes obesity is relatively unexplored. Also, surviving Prox1 heterozygous mice have shown abnormal lymphatic patterning and adult-onset obesity, indicating that accumulation of adipocytes could be closely linked with lymphatic function. Here, we propose a new antiobesity strategy based on enhancement of lymphatic and blood vessel integrity with apelin. Apelin knockout (KO) mice fed a high-fat diet (HFD) showed an obese phenotype associated with abnormal lymphatic and blood vessel enlargement. Fatty acids present in the HFD induced hyperpermeability of endothelial cells, causing adipocyte differentiation, whereas apelin promoted vascular stabilization. Moreover, treatment of apelin KO mice with a selective cyclooxygenase-2 inhibitor, celecoxib, that were fed an HFD improved vascular function and also attenuated obesity. Finally, apelin transgenic mice showed decreased subcutaneous adipose tissue attributable to inhibition of HFD-induced hyperpermeability of vessels. These results indicate that apelin inhibits HFD-induced obesity by enhancing vessel integrity. Apelin could serve as a therapeutic target for treating obesity and related diseases. ***Diabetes* 62:1970–1980, 2013**

Obesity appears to be associated with a combination of genetic susceptibility, increased consumption of high-energy foods, and decreased physical activity, leading to excessive accumulation of white adipose tissues that serve to store surplus energy in the form of lipid within adipocytes (1). It is correlated with type 2 diabetes, cardiovascular disease, and certain types of cancer, and therefore represents a serious public health problem. Although the molecular mechanisms underlying obesity have not been fully clarified, effective therapeutic approaches are needed.

The blood and lymphatic systems are composed of dense networks of capillaries. Blood vessels are indispensable to import and carry fluid, dissolved proteins, and cells into interstitial space, whereas lymphatic vessels drain protein-rich lymph and traffic immune cells from the extracellular space (2). Adipose tissue is mainly composed of adipocytes surrounded by stromal vascular tissue. The balance of adipokine production is disrupted by excess adipose tissue, leading to chronic vascular inflammation, which in turn may lead to cardiovascular disease (3). The outgrowth of adipose tissue is tightly correlated with angiogenesis (4). Thus, antiangiogenesis therapy has emerged as a potential treatment of obesity. However, this idea remains controversial not only because angiogenesis is physiologically important but also because brown adipose tissue consumes more energy if angiogenesis is increased (5). Moreover, there is an increasing emphasis on lymphatic function in obesity research. *Chy* mice, a naturally occurring mouse model of lymphedema attributable to heterozygous inactivating mutations in vascular endothelial growth factor receptor (VEGFR)-3, exhibit adipose layer accumulation (6). Also, surviving Prox1 heterozygous mice show abnormal lymphatic patterning and adult-onset obesity (7). Thus, accumulation of adipocytes could be closely linked with the structure and function of lymphatic vessels. However, little is known about how vessel integrity influences adipocyte dynamics.

The apelin gene encodes a 77-amino-acid preprotein, which is cleaved to shorter active peptides that bind to the apelin receptor (APJ), a G-protein-coupled receptor (8). The full-length mature peptide comprises 36 amino acids (apelin-36), and other active fragments, including a 13-amino-acid peptide known as apelin-13, also are formed. Apelin is expressed widely in the vascular endothelium and acts both locally and via endocrine signaling to activate APJ, which is expressed in cardiomyocytes, endothelial cells, and vascular smooth muscle cells (9). Apelin/APJ signaling is located downstream of angiopoietin-1/Tie2 signaling in endothelial cells (10). Apelin transgenic mice develop enlarged, but not leaky, blood vessels in ischemia, leading to functional recovery (11). More recently, we have shown that apelin attenuates edema formation and inflammation by promoting lymphatic function in vivo (12).

Herein, we show that the apelin/APJ system enhances the integrity of lymphatic and blood vessels exposed to dietary fatty acids, resulting in inhibition of high-fat diet (HFD)-induced obesity. These results suggest that apelin may be a new therapeutic target in the treatment of obesity and its related diseases.

RESEARCH DESIGN AND METHODS

Animals. Male and female apelin-deficient mice (knockout [KO]) and apelin transgenic mice under the control of keratin 14 on a C57/BL6 background (K14-apelin) were generated as described previously (11). All animals were housed in groups (n = 3–10) in a temperature-controlled room with a 12-h/12-h light–dark cycle. Both wild-type (WT) and KO mice (7–11 weeks old) were maintained on HFD (D12492, 60 kcal % fat; Research Diets, New Brunswick, NJ) for 17 weeks. In other studies, WT and KO mice fed the same HFD were further divided into two groups (n = 3–7) cotreated with vehicle or 0.1% selective cyclooxygenase (COX) 2 inhibitor celecoxib (CEL; LC Laboratories, Woburn, MA) from the age of 7–8 weeks for 8 weeks. Moreover, K14-apelin and WT mice at age 4–5 weeks were fed HFD (D12451, 45 kcal % fat; Research Diets)

From the [1]Department of Signal Transduction, Research Institute of Microbial Diseases, Osaka University, Osaka, Japan; and the [2]Shiseido Innovative Science Research Center, Yokohama, Japan.
Corresponding author: Kentaro Kajiya, kentaro.kajiya@to.shiseido.co.jp, or Nobuyuki Takakura, ntakaku@biken.osaka-u.ac.jp.
Received 9 May 2012 and accepted 25 January 2013.
DOI: 10.2337/db12-0604

for 8 weeks. Mice had free access to food and water. We measured body weight and the mass of food consumed every week. At the end of the study, we weighed the inguinal and mesenteric fat pads and collected the ears, back skin, and mesenteric fat for histological analysis, and collected blood samples for analysis of the circulating levels of glucose, triglyceride, free fatty acids, HDL cholesterol, insulin, leptin, and adiponectin. Plasma of HR-1 hairless mice fed a regular diet (RD; CRF-1; Oriental Yeast, Tokyo, Japan) or HFD (D12492, 60 kcal % fat; Research Diets) for 11 weeks also was collected. The current study was approved by the Ethics Committee of Shiseido Research Center in accordance with the guidelines of the National Institute of Health.

Immunohistochemical and computer-assisted morphometric vessel analysis. Immunofluorescence analysis was performed on 6-μm cryostat sections of mouse back skin or 12-μm cryostat sections of mesenteric fat using antibodies against the macrophage monocyte marker CD11b (BD Biosciences, Bedford, MA), the blood vessel–specific marker meca-32 (BD Biosciences), the lymphatic-specific marker LYVE-1 (MBL, Nagoya, Japan), podoplanin (AngioBio, Del Mar, CA), APJ (10), perilipin (PROGEN Biotechnik GmbH, Heidelberg, Germany), Ki-67 antigen (Dako Cytomation, Glostrup, Denmark), and corresponding secondary antibodies labeled with AlexaFluor488 or AlexaFluor594 (Molecular Probes, Eugene, OR). Routine hematoxylin and eosin staining also was performed. Sections were examined with an Olympus AX80T microscope (Olympus, Tokyo, Japan) and images were captured with a DP-controlled digital camera (Olympus). Morphometric analyses were performed using the IP-LABORATORY software as described (13). Three different fields of each section were examined and the number of macrophages and the average vessel size in the dermis and in the mesenteric fat were determined. Whole-mount immunohistochemical analysis of ear skin was performed. Tissues were incubated in 30% H_2O_2, 3% normal goat serum (Invitrogen, Camarillo, CA), and 0.25% Triton X-100 in PBS, and incubated overnight at 4°C with anticlaudin-5 antibody (Santa Cruz Biotechnology, Santa Cruz, CA) or anti-CD31 antibody (BD Biosciences), as an endothelial marker, and anti-podoplanin antibody (AngioBio, Del Mar, CA) or anti-LYVE-1 antibody, as a lymphatic marker. Then, corresponding secondary antibodies labeled with AlexaFluor488 or AlexaFluor594 (Molecular Probes) were applied. Specimens were viewed with a LSM5 Pascal confocal laser-scanning microscope (Carl Zeiss, Thornwood, NY).

Adipose tissue imaging. Adipose tissue imaging of inguinal fat was performed as described previously (14). The inguinal subcutaneous fat was minced into small pieces and incubated with BODIPY (4,4-difluoro-3a,4a-diaza-s-indacene) conjugated with Alexa Fluor (Invitrogen-Molecular Probes, Carlsbad, CA) as a lipid droplet marker and Isolectin IB_4 Alexa Fluor dye conjugates (Invitrogen-Molecular Probes) as an endothelial marker. The three-dimensional structure of adipocytes was observed using a LSM5 Pascal confocal laser-scanning microscope (Carl Zeiss). Adipocyte diameter was determined using IPLab software. Four image fields were acquired from three animals in each group, and the diameters of 20 cells in each field were measured by an observer blinded regarding the status of the sample. Adipocytes were defined as regular, round, $BODIPY^+$ cells without plasma membrane disruption.

Blood analysis. Plasma glucose, HDL cholesterol, and triglyceride levels were measured using a Fuji DRI-CHEM analyzer (Fuji Film, Tokyo, Japan). Plasma free fatty acid level was determined with a Wako NEFA C test kit (Wako Chemicals, Neuss, Germany). Insulin, leptin, and adiponectin were assayed with a mouse insulin ELISA kit (Shibayagi, Gunma, Japan) and a leptin and adiponectin ELISA kit (R&D Systems, Minneapolis, MN), respectively, according to the manufacturers' instructions.

Plasma extravasation and lymphatic functional analysis. To examine the blood vascular permeability, Miles assay was performed as previously described (11). Briefly, mice were anesthetized and intravenously injected with 100 μL of a 1% solution of Evans blue dye in 0.9% NaCl. At 30 min after dye injection, pictures were taken and the epididymal fat was removed. The dye was eluted from dissected samples with formaldehyde at 56°C and the optical density was measured by spectrophotometry (Biotrak II; GE Healthcare, Fairfield, CT) at 620 nm. For lymphatic functional analysis, a 1-μl aliquot of 1% solution of Evans blue dye in 0.9% NaCl was injected intradermally at the inner surface of the rim of the ear using a 10-μL Hamilton syringe; this is a standard method to macroscopically visualize cutaneous lymphatic vessels and lymphatic drainage. Mouse ears were photographed at 1 and 5 min after the dye injection. Additionally, 100 μL of 1% solution of Evans blue dye in 0.9% NaCl was injected into the stomach and at 30 min after dye injection, the mesenteric fat was carefully removed from the intestine. The optical density of the eluted dye in the mesenteric fat was measured.

Cells. Human dermal lymphatic endothelial cells (LECs) were isolated from neonatal human foreskins by immunomagnetic purification as described previously (15). Lineage-specific differentiation was confirmed by real-time RT-PCR for the lymphatic vascular markers Prox1, LYVE-1, and podoplanin, as well as by immunostaining for Prox1 and podoplanin as described (13). Human umbilical vein endothelial cells were purchased (PromoCell, Heidelberg, Germany) and cultured in endothelial basal medium (Lonza, Verviers, Switzerland) with supplements provided by the suppliers for up to 11 passages. Primary human subcutaneous preadipocytes (Lonza) were cultured as recommended by the supplier in preadipocyte basal medium 2 containing 10% FBS, 2 mmol/L L-glutamine, and antibiotics. The 3T3-L1 preadipocytes were cultured in DMEM with 10% FBS and antibiotics.

Permeability assay. LECs and human umbilical vein endothelial cells were grown to confluence on the fibronectin-coated surface of 0.4-μm pore-size tissue culture inserts (Corning, Lowell, MA). Oleate (20 or 100 μmol/L) and steareate (20 or 100 μmol/L) were placed into the upper and lower chambers for 5 h after incubation with apelin-13 (1,000 ng/mL) or a selective COX2 inhibitor, CEL (1 μmol/L), for 1 h. FITC-dextran was added to the upper chambers, and the apparatus was then placed in a CO_2 incubator at 37°C. After incubation for 15 min, a 100-μL sample was taken from the lower chamber and the absorbance of FITC-dextran was determined at 492 nm using a spectrophotometer (Fluoroskan Ascent; Thermo Fisher Scientific, Waltham, MA).

Adipocyte differentiation assay. Differentiation of 3T3-L1 preadipocytes was performed by treatment with insulin, dexamethasone, and 3-isobutyl-1-methylxanthine in DMEM with 10% FBS for 2 days as described (16). Then, the medium was replaced with DMEM containing 10% FBS and insulin before coculture with LECs. Coculture was performed by incubating LECs to confluence on the 0.4-μm pore-size cell culture insert (Corning) and placing them in 6-well plates containing 3T3-L1 adipocytes differentiated for 2 days; 0.5% plasma from mice fed RD or HFD for 11 weeks was added to the upper chambers. After incubation for 7 days, the cells in the lower wells were stained with Oil-Red-O (Wako Pure Chemical Industry, Osaka, Japan) as described previously (17). The stained lipids present in the mature adipocytes were solubilized with isopropanol and measured spectrophotometrically at 510 nm. To induce differentiation of human preadipocytes into mature adipocytes, confluent preadipocytes in plates were cultured in preadipocyte basal medium 2 plus 10% FBS, 2 mmol/L glutamine, and antibiotics for 2 days and then switched to preadipocyte basal medium 2 plus 10% FBS, 2 mmol/L glutamine, antibiotics, 10 μg/mL insulin, 500 μmol/L isobutylmethylxanthine, 1 μmol/L dexamethasone, and 200 μmol/L indomethacin in the presence or absence of oleate (100 μmol/L) and steareate (100 μmol/L). After 9 days of incubation, cells were fixed with 10% formaldehyde, stained with Oil-Red-O (Wako Pure Chemical Industry) and observed under a bright-field microscope (Olympus) as described previously (17).

Immunofluorescence microscopy. LECs and human umbilical vein endothelial cells were seeded on cover slips and incubated until confluence. For the detection of VE-cadherin, cells were fixed with 1% PFA and incubated with anti-VE-cadherin antibody (R&D Systems, Minneapolis, MN). AlexaFluor594-labeled secondary antibody was used for fluorescence detection. All images were acquired using a DP-controlled digital camera (Olympus) on an Olympus AX80T microscope (Olympus).

Quantitative real-time RT-PCR. Total RNAs were isolated from LECs cultured in the presence or absence of apelin (1,000 ng/mL) for 4 h after serum starvation. The expression of COX2 mRNA was examined by quantitative real-time RT-PCR using a LightCycler 480 (Roche Applied Science, Indianapolis, IN). The primers for COX2 were as follows: forward primer, 5′- TAGAGCCCTTCCTCCTGTGC-3′, and reverse primer, 5′- CTGGGCAAAGAATGCAAACA-3′. Expression levels were normalized with respect to β-actin as an internal control (forward primer: 5′-TCACCGAGCGCGGCT-3′; reverse primer: 5′-TAATGTCACGCACGATTTCCC-3′).

Statistical analysis. All data are expressed as means ± SD and as the statistical significance of differences with an unpaired *t* test.

RESULTS

Disruption of apelin/APJ signaling in vivo promotes obesity. To investigate the physiological role of apelin in obesity, apelin KO mice were fed HFD. Surprisingly, after 5 weeks of HFD, apelin KO mice showed increased body weight compared with WT littermates (Fig. 1*A*); at the end of the feeding period, the body weight gains were 20 ± 0.5 g for WT mice and 30 ± 0.5 g for apelin KO mice ($P < 0.01$) (Fig. 1*B*). As expected, both inguinal subcutaneous and mesenteric fat depots were significantly increased by HFD in apelin KO mice compared with WT mice (Fig. 1*C*, *D*). Moreover, hematoxylin and eosin staining revealed a thickened subcutaneous adipose layer in the skin of HFD-fed apelin KO mice as compared with WT mice (Fig. 1*E*). To visualize the three-dimensional structure of adipose tissue, we used fluorescence staining with BODIPY, which recognizes intercellular lipid droplets in

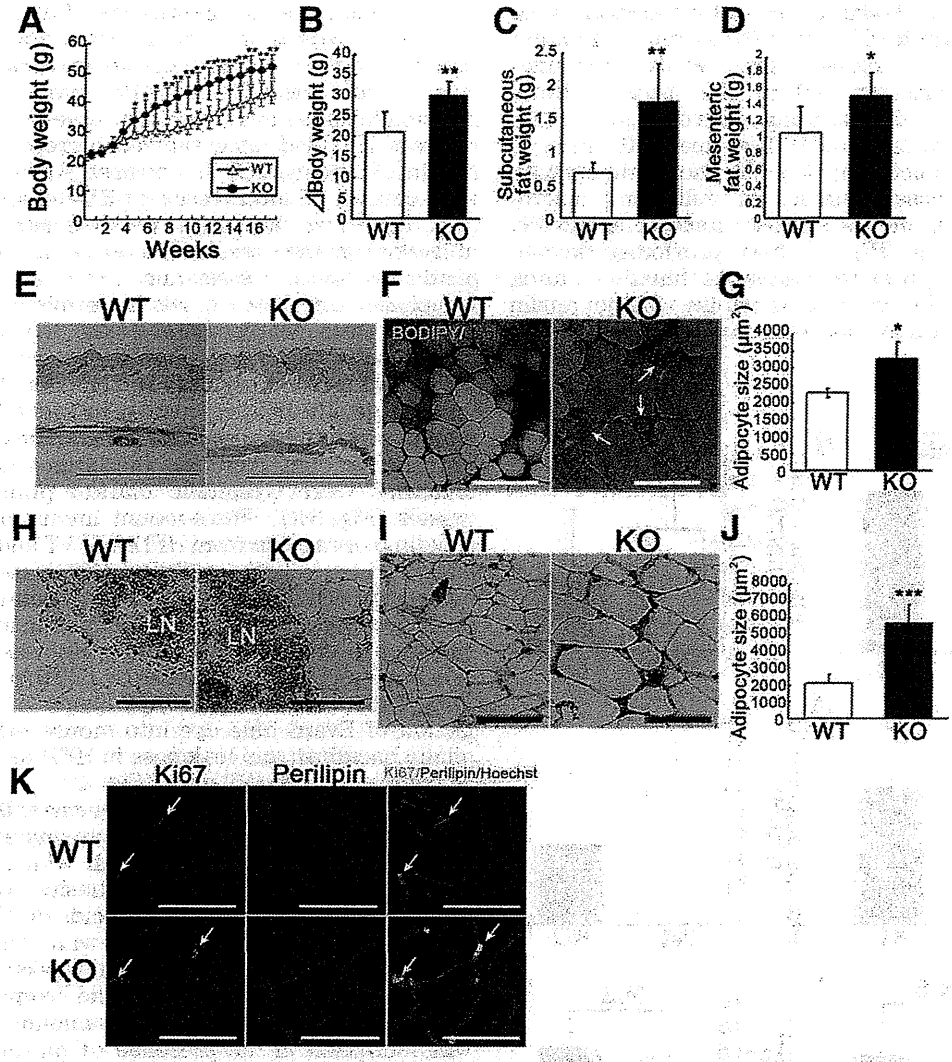

FIG. 1. Obesity in HFD-fed apelin KO mice. *A*: Body weight of HFD-fed apelin KO and WT mice ($N = 7$). Increased body weight (*B*), inguinal subcutaneous fat weight (*C*), and mesenteric fat weight (*D*) in apelin KO mice after 17 weeks of HFD. *E*: Hematoxylin and eosin staining showed a thickened subcutaneous fat layer in apelin KO mice. BODIPY (green) and Isolectin (red) staining revealed increased lipid droplet (green) size in subcutaneous adipocytes in apelin KO mice (*F*). Morphometric analysis of adipocyte size confirmed enlargement of adipocytes in apelin KO mice (*G*). Arrows show crown-like structures in obese fat pads. Hematoxylin and eosin staining of subcutaneous adipose tissue surrounding lymph nodes (LN) (*H*) and of mesenteric fat tissue (*I*). *J*: Morphometric analysis of mesenteric adipocyte size. Bars indicate 200 μm except in (*E*), which shows 1 mm. Date are expressed as mean values ± SD. *K*: Double immunofluorescence staining with Ki67 (green) and perilipin (red) in the mesenteric fat of WT and apelin KO mice after HFD. Arrows show proliferating adipocytes. ***$P < 0.001$, **$P < 0.01$, *$P < 0.05$.

adipocytes. Subcutaneous adipocytes in HFD-fed apelin KO mice were increased in size (Fig. 1*F*) and surrounded by endothelial cells, which appeared to form crown-like structures in obese fat pads, as described previously (14). Morphometric analysis confirmed that adipocytes were enlarged in the HFD-fed apelin KO mice (Fig. 1*G*). Sections of subcutaneous white adipose tissue around lymph nodes and sections of mesenteric fat tissue showed increased adipocyte size of apelin KO mice as compared with controls (Fig. 1*H–J*). Double immunofluorescence staining using antibodies against proliferation marker Ki67 and perilipin revealed no significant difference of proliferating adipocytes in mesenteric fat tissues between apelin KO mice and WT mice after HFD (Fig. 1*K*).

No major abnormality of food consumption or lipid metabolism in apelin KO mice. Because apelin/APJ signaling in the central nervous system contributes to body fluid homeostasis (18), we investigated the food consumption of HFD-fed apelin KO mice to determine if the obese phenotype of apelin KO mice was elicited by abnormality of hypothalamic function after HFD feeding. There was no significant difference in the amount of weekly food intake between apelin KO mice and their WT littermates (Fig. 2*A*). The plasma insulin level in obese apelin KO mice was slightly, but not significantly, decreased as compared with WT mice (Fig. 2*B*). However, the leptin concentration in apelin KO mice was significantly increased, whereas the adiponectin level was significantly decreased (Fig. 2*C*, *D*). We also measured the levels of circulating glucose, HDL cholesterol, triglycerides, and free fatty acids in the plasma of obese apelin KO mice and their WT counterparts but found no significant difference in any of these factors (Fig. 2*E–H*).

Abnormal lymphatic dysfunction and inflammation in skin of HFD-fed apelin KO mice. To examine infiltration of macrophages in the adipose tissue, we used immunohistochemical staining for CD11b. The results demonstrated an increase of infiltrating macrophages in the subcutaneous adipose layer of HFD-fed apelin KO mice, as compared with WT mice (Fig. 3*A*). Morphometric analysis confirmed an increased number of infiltrating macrophages in the subcutaneous adipose tissue of apelin KO mice ($P < 0.01$) (Fig. 3*B*). We have previously demonstrated that apelin promotes lymphatic function during inflammation (12). Therefore, to determine whether apelin depletion could lead to vascular abnormality in obese mice, we examined the expression of the APJ in lymphatic and blood vessels in vivo. Double immunofluorescence staining for the lymphatic marker podoplanin or the vascular marker meca-32 and APJ revealed weak APJ expression in cutaneous lymphatic vessels from mice fed RD, whereas HFD-fed mice showed increased expression of APJ in LECs (Fig. 3*C*). In contrast, APJ expression levels were similar in blood vessels of RD-fed and HFD-fed mice (Fig. 3*D*). Given these data, we speculated that disruption of apelin signaling resulted in abnormal structure of lymphatic or blood vessels and increased their leakiness. Lymphatic and blood vessels in dermis of HFD-fed apelin KO mice were clearly enlarged (Fig. 3*E*), and the diameter of lymphatic and blood vessels was increased compared with those in WT controls (Fig. 3*F*). In addition, to analyze the enlarged lymphatic structure in apelin KO mice, whole-mount immunofluorescence for claudin-5 also was performed. We confirmed that the large vessels stained for claudin-5 were lymphatic marker podoplanin-positive vessels (Fig. 3*G*). Whole-mount immunofluorescence for claudin-5 of ear skin from HFD-fed WT and apelin KO mice also revealed dilation of lymphatic vessels in apelin KO mice (Fig. 3*G*). Surprisingly, obese apelin-KO mice showed not only angiogenesis but also lymphatic hyperplasia in the subcutaneous fat layer, whereas this was not the case in subcutaneous adipose tissue of HFD-fed WT mice (Fig. 3*H*). Functional analyses by means of intradermal injection of Evans blue dye into mouse ears revealed lymphatic backflush and leakiness in HFD-fed apelin KO mice as compared with WT mice (Fig. 3*I*).

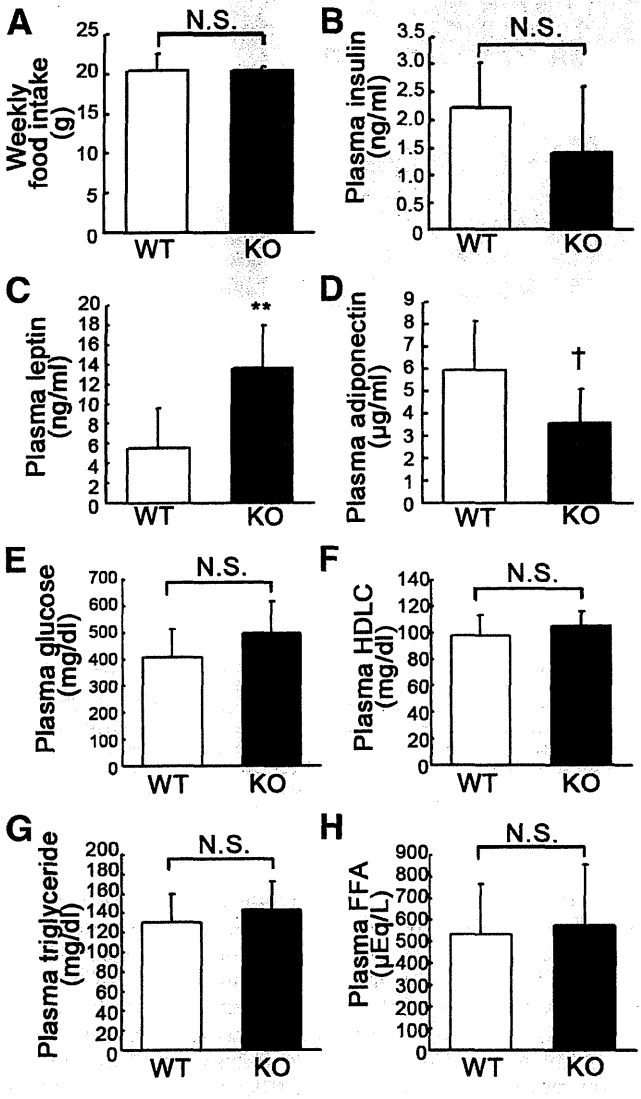

FIG. 2. No significant difference was found in food consumption or lipid metabolism between apelin KO and WT mice after HFD. *A*: Food intake was similar in apelin KO mice and WT littermates. *B*: Obese apelin KO mice had a lower plasma insulin level, but the difference was not significant. *C*: Serum leptin levels were approximately two times higher in apelin KO mice than in WT mice (**$P < 0.01$). *D*: Serum adiponectin levels tended to be lower in apelin KO mice, but the difference was not significant. There was no significant difference of plasma glucose (*E*), HDL cholesterol (HDLC; *F*), triglyceride (*G*), or free fatty acid (FFA; *H*) between apelin KO mice and WT mice. Data are expressed as mean values ± SD ($N = 7$; **$P < 0.01$, †$P < 0.1$). N.S., not significant.

Dietary fatty acids cause hyperpermeability of lymphatic and blood vessels and adipocyte hypertrophy. To understand the mechanism through which HFD-fed apelin KO mice developed significant obesity, we investigated in vitro the effects of dietary fatty acids on LECs. The 3T3-L1 preadipocytes were cocultured with confluent LECs on Transwell inserts in the presence of plasma from HFD-fed or RD-fed WT mice to mimic the lymphatic endothelial wall (Fig. 4*A*). Surprisingly, the amount of lipid droplets was increased in the presence of plasma from HFD-fed mice, whereas no major difference was found in the presence or absence of plasma from RD-fed mice (Fig. 4*B*, *C*). Because significant increases of oleic acid and stearic acid were found in plasma of HFD-fed mice (M. Takagi, unpublished observation), we speculated that the elevated fatty acids in plasma of HFD-fed mice would induce dysfunction of lymphatic and blood vessels via apelin depletion, thereby promoting obesity. Treatment of LECs with 20 and 100 μmol/L oleic acid resulted in hyperpermeability of LECs compared with untreated cells (Fig. 4*D*). Moreover, we confirmed that these dietary fatty acids promoted differentiation of human subcutaneous adipocytes (Fig. 4*E*). Preincubation with apelin-13 blocked the hyperpermeability of lymphatic and blood vessel endothelial cells induced by oleic acid (Fig. 4*F*, *G*). Moreover, whereas unstimulated endothelial cells were stained evenly with VE-cadherin at sites of cell–cell junctions, cells incubated with oleic acid displayed discontinuous staining with considerable gaps. Surprisingly, cells pretreated with apelin-13 before incubation with oleic acid retained the normal staining pattern of VE-cadherin (Fig. 4*H*). These data indicate that the oleic acid in HFD enhances the leakiness of lymphatic and vascular structures via disruption of VE-cadherin, and that leakage of dietary fatty acids from the vessels mediates adipocyte hypertrophy.

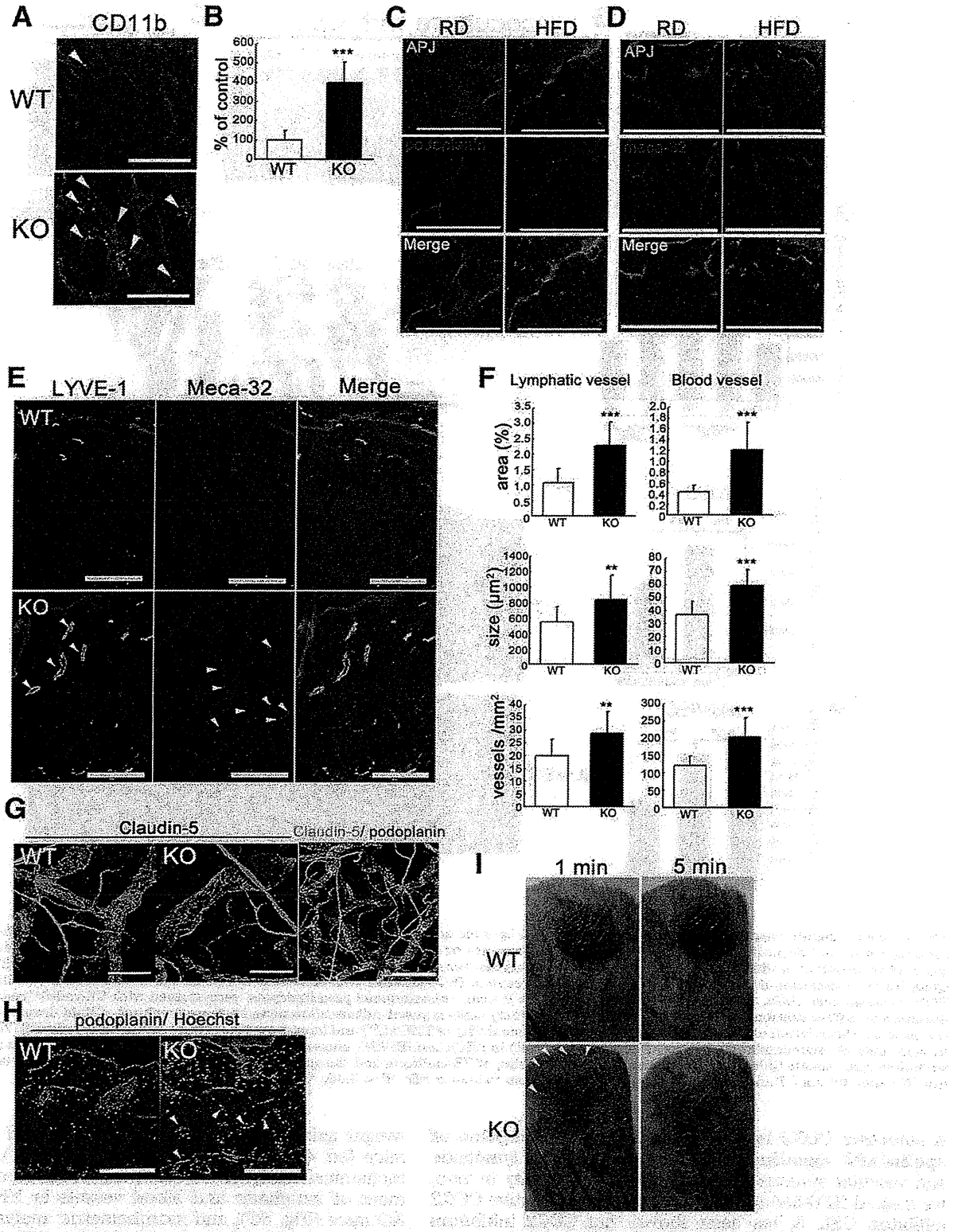

FIG. 3. Enhanced inflammation and vascular malformation in obese apelin KO mice. *A*: Increased CD11b$^+$ macrophages (green) in the subcutaneous adipose layer of skin from apelin KO mice. *B*: Morphometric analysis showed that the number of CD11b$^+$ macrophages was significantly increased in apelin KO mice. Double immunofluorescence staining for podoplanin (*C*, red) or meca-32 (*D*, red) and for APJ (green) revealed upregulated expression of APJ in lymphatics of skin of HFD-fed mice. *E*: Double immunofluorescence staining of skin for LYVE-1 (green) and meca-32 (red) revealed enlargement (arrowheads) and enhanced formation of LYVE-1$^+$ lymphatic vessels and meca-32$^+$ blood vessels in apelin KO mice. *F*: Computer-assisted morphometric analyses of lymphatic and blood vessels in skin. *G*: Immunofluorescence staining for claudin-5 in a whole-mount of ear skin. Lymphatic vessels in apelin KO mice were partly dilated compared with controls. Double immunofluorescence staining of claudin-5 (green) and podoplanin (red) confirmed that the nonuniform vessels were podoplanin-positive lymphatic vessels. *H*: Immunofluorescence analysis of mouse skin for podoplanin (red) revealed lymphatic hyperplasia in the adipose layer of apelin KO mice. *I*: Intradermal injection of Evans blue dye visualized enhanced leakiness of enlarged lymphatic vessels and lymphatic backflush (arrowheads) in apelin KO mice at 1 and 5 min after the injection. Scale bars indicate 200 μm except in (*G*), which indicates 100 μm. Data are expressed as mean values ± SD. $^{**}P < 0.01$, $^{***}P < 0.001$.

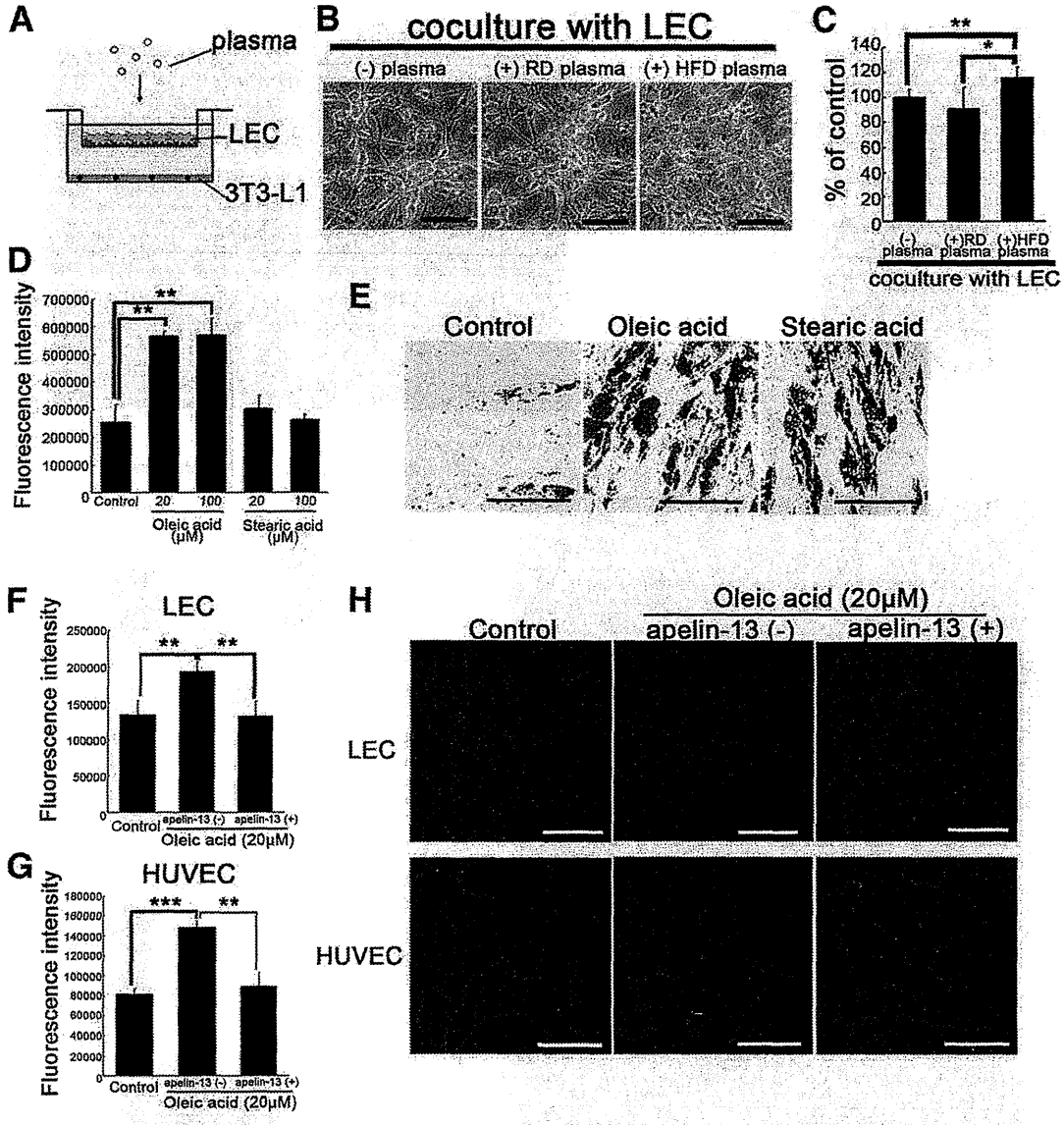

FIG. 4. Apelin inhibits vascular hyperpermeability induced by oleic acid, thereby blocking adipocyte differentiation. *A*: Schematic illustration of coculture study of LECs with 3T3-L1 preadipocytes in the presence or absence of plasma. Confluent LECs were inserted with or without plasma on day 2 after initiation of differentiation. *B*: 3T3-L1 preadipocytes were stained with Oil-red-O (red) on day 9 after initiation of differentiation. *C*: Quantitative evaluation of lipid droplets of 3T3-L1 preadipocytes. *D*: Treatment with oleic acid increased the fluorescence intensity of permeated FITC-dextran from LECs, as compared with the control. *E*: Human subcutaneous preadipocytes were stained with Oil-red-O (red) on day 9 after initiation of differentiation with oleic acid or stearic acid. Fatty acid–exposed culture showed an increased amount of lipid droplets compared with the control. The addition of apelin-13 blocked the hyperpermeability of LECs (*F*) and human umbilical vein endothelial cells (HUVECs; *G*) induced by oleic acid. *H*: Immunohistochemistry of VE-cadherin (red) in LECs and HUVEC, showing discontinuous staining of VE-cadherin after incubation with oleic acid. Apelin-13 blocked the discontinuity of staining of VE-cadherin and the gap formation induced by oleic acid. Scale bars indicate 200 μm (*E*) and 100 μm (*B* and *H*). Data are expressed as mean values ± SD. *$P < 0.05$, **$P < 0.01$, ***$P < 0.001$.

A selective COX2 inhibitor blocked the disruption of apelin/APJ signaling. To determine how the lymphatic and vascular systems affect HFD-induced obesity in vivo, we treated HFD-fed apelin KO mice with a selective COX2 inhibitor, CEL. It has been shown that COX2 inhibitors block angiogenesis and lymphangiogenesis during tumor growth (19). The CEL-treated, HFD-fed, apelin KO mice gained 30% less weight than HFD-fed apelin KO mice, and showed differences in subcutaneous and mesenteric fat accumulation (Fig. 5*A–D*). Hematoxylin and eosin staining of skin sections confirmed a decreased adipose layer in the CEL-treated apelin KO mice, with a decreased adipocyte diameter (Fig. 5*E*, *F*). However, no significant difference in weight gain or fat accumulation was found between WT mice fed with and without CEL (Fig. 5*A–D*). Immunohistochemical analyses revealed that CEL blocked enlargement of lymphatic and blood vessels in HFD-fed apelin KO mice (Fig. 5*G*), and morphometric analysis confirmed that the vessel size was decreased (Fig. 5*H*). Moreover, fat pads from CEL-treated, HFD-fed, apelin KO mice showed decreased $CD11b^+$ macrophages (Fig. 5*I*). CEL-treated, HFD-fed, apelin KO mice showed a decreased number of macrophages in subcutaneous adipose tissue (Fig. 5*J*). Further, CEL blocked the lymphatic and blood vascular hyperpermeability induced by oleic acid, like apelin-13 (Fig. 5*K*). In contrast, COX2 expression in LECs was

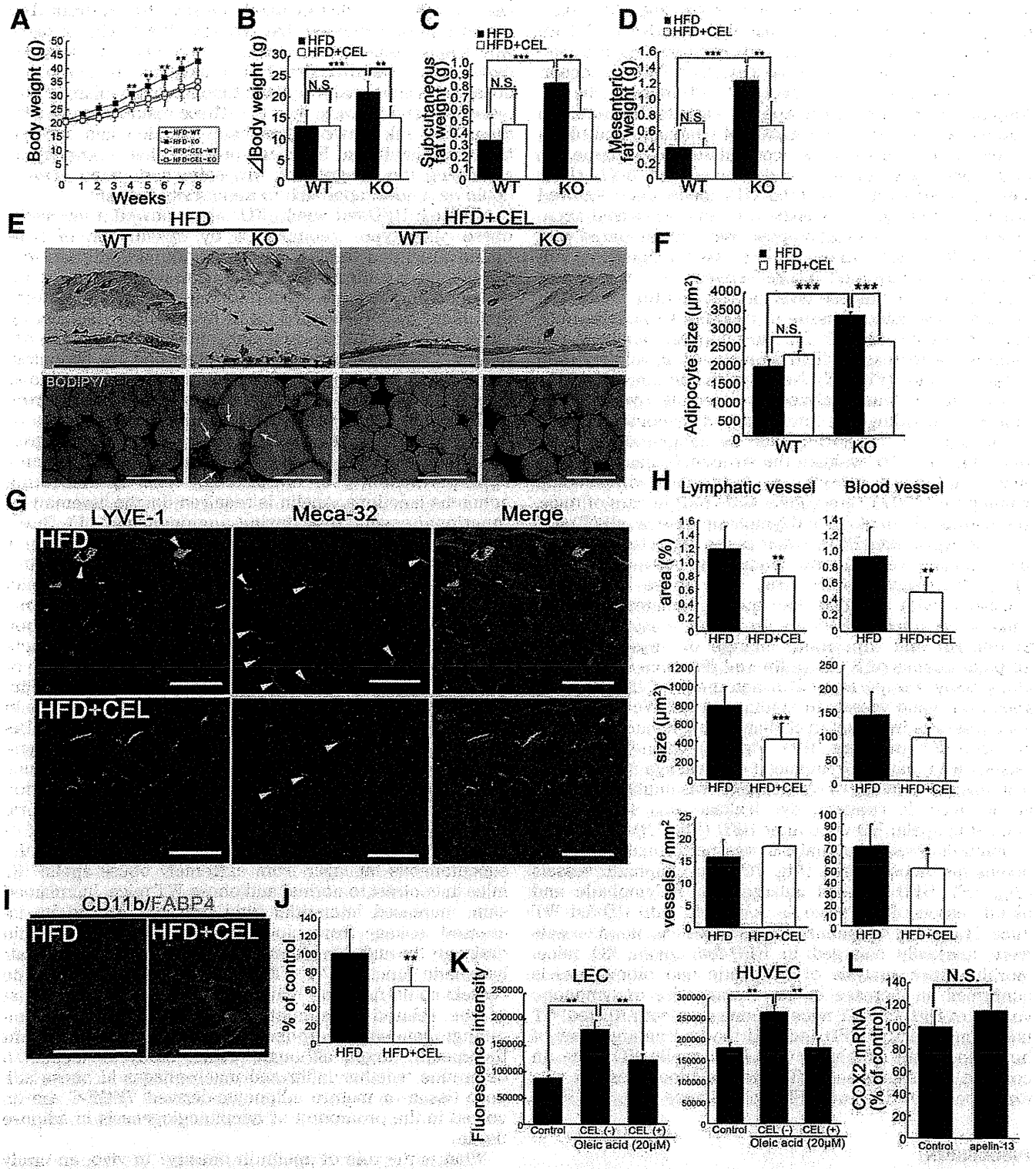

FIG. 5. Obesity induced by apelin depletion after HFD was blocked by orally administered selective COX2 inhibitor. A: Weight gain in WT and apelin KO mice maintained on HFD or HFD containing CEL (N = 3–7). The change of body weight (B) and tissue weight of inguinal subcutaneous (C) and mesenteric (D) fat after HFD or HFD with CEL. E: Histological analysis of skin and subcutaneous adipose tissue imaging using BODIPY (green) and Isolectin (red) showed that hypertrophic adipocytes (green) were reduced in CEL-treated HFD-fed apelin KO and WT mice. Arrows show crown-like structures in obese fat pads. F: Mean adipocyte size in CEL-treated, HFD-fed, apelin KO mice was smaller than in HFD-fed apelin KO mice. G: Immunohistochemical analyses for LYVE-1 (green) and meca-32 (red) revealed that enlargement of lymphatic and blood vessels (arrowheads) in the skin of HFD-fed apelin KO mice was inhibited by CEL. H: Morphometric analyses of lymphatic and blood vessels in CEL-treated, HFD-fed, apelin KO mice and HFD-fed apelin KO mice. I: Double immunofluorescence staining for CD11b (red) and FABP4 (green) showed that macrophage infiltration in the subcutaneous fat layer from HFD-fed apelin KO mice was blocked by CEL. J: The number of infiltrated macrophages was decreased in apelin KO mice fed HFD with CEL. K: Increased permeability in LECs and human umbilical vein endothelial cells (HUVECs) after the treatment with oleic acid was blocked by the addition of CEL. Bars indicate 1 mm (E, top) and 200 μm (E, bottom, G, and I). Data are expressed as mean values ± SD. L: COX2 expression after apelin treatment of LECs. ***$P < 0.001$, **$P < 0.01$, and *$P < 0.05$.

similar in controls and apelin-treated cells (Fig. 5*L*). Taken together, these results show that the selective COX2 inhibitor CEL ameliorated both inflammation and the dysfunction of lymphatic and blood vessels in HFD-fed apelin KO mice, resulting in the inhibition of HFD-induced obesity.

Resistance to obesity in apelin transgenic mice. To examine whether the stabilization of lymphatic and blood vessels by apelin inhibits the accumulation of fat tissue, we used apelin transgenic mice under the control of K14 (K14-apelin). Interestingly, HFD-fed K14-apelin mice showed significant inhibition of weight gain and decreased accumulation of subcutaneous adipose tissue as compared with HFD-fed WT mice, although there was no significant difference of weekly food intake between the two groups (Fig. 6*A*, *B*). The adipose layer of skin and the amount of subcutaneous adipose tissue in HFD-fed K14-apelin mice were decreased (Fig. 6*C*, *D*). Morphometric analysis also confirmed a decrease of lipid droplets within adipocytes in K14-apelin mice (Fig. 6*E*). Next, lymphatic function in the mesenteric fat was analyzed by injecting dye into the stomach, revealing the inhibition of lymphatic hyperpermeability in K14-apelin mice as compared with WT mice (Fig. 6*F*). To evaluate the structural change of lymphatic and blood vessels, we performed whole-mount staining for LYVE-1 (green)/meca-32 (red) in ears of mice. Interestingly, both blood and lymphatic vessels of WT mice were enlarged after HFD, whereas the diameters of blood and lymphatic vessels were comparable between RD- and HFD-fed K14-apelin mice (Fig. 6*G*). These results are consistent with the idea that apelin regulates the accumulation of adipose tissue by promoting vessel integrity.

Structural and functional change of vessels in the adipose tissues of K14-apelin and KO mice after HFD. Miles assay was performed to determine of the effect of apelin on blood vessels in epididymal fat. We found that leakiness was inhibited in K14-apelin mice and enhanced in apelin KO mice after HFD (Fig. 7*A*). Quantitative analysis showed that HFD enhanced dye leakage in WT mice, whereas the increase of dye leakage was inhibited in K14-apelin mice. In contrast, dye leakage was strongly enhanced in apelin KO mice after HFD (Fig. 7*B*).

Immnofluorescence analysis was performed with antibodies for blood vessels (Fig. 7*C*) and lymphatic vessels (Fig. 7*E*). HFD induced enlargement of lymphatic and blood vessels of WT mice as compared with RD-fed WT mice. Moreover, lymphatic vessels as well as blood vessels were markedly enlarged in HFD-fed apelin KO mice. Morphometric analysis of lymphatic and blood vessels confirmed an increase in the average size of lymphatic vessels of HFD-fed WT mice as compared with RD-fed WT mice. Importantly, HFD induced marked enlargement of both blood and lymphatic vessels in apelin KO mice. In contrast, no significant difference of blood vessels was found between RD- and HFD-fed WT mice (Fig. 7*D*, *F*).

DISCUSSION

Our results indicate that apelin/APJ signaling plays a crucial role in the control of fat accumulation by enhancing the integrity of lymphatic and blood vessels. It is well-established that fat intake is associated with the growth of adipose tissue vasculature. This, in turn, suggests that inhibition of angiogenesis in adipose tissue could be an approach to treat obesity, but this idea is controversial because of the physiological importance of angiogenesis. It was reported that partial blockade of the VEGFR pathway had no effect on diet-induced obesity (5). Additionally, recent reports indicated that blocking the VEGFR-3 pathway in skin resulted in an increase of subcutaneous adipose tissue (20), and that Prox1 heterozygous mice showed obesity and abnormal lymphatic function, particularly at the mesentery and thoracic duct (7). These results suggest that there is a link between lymphatic function and adipose tissue accumulation. Here, we propose that a strategy of enhancing the integrity of lymphatic and blood vessels could be a novel approach to antiobesity therapy.

Although HFD-fed apelin KO mice showed a markedly obese phenotype accompanied by dysfunction of lymphatic and blood vessels, it was also found that there was no significant difference of either vessel function or fat accumulation between apelin KO and WT mice fed a normal diet. These results led us to hypothesize that dietary fatty acids accelerate vascular damage via apelin depletion, because fatty acids are absorbed by lymphatic vessels and transported to peripheral tissues by blood vessels. Our in vitro study demonstrated that plasma from HFD-fed mice increased the amount of lipid droplets of 3T3-L1 preadipocytes by disrupting lymphatic integrity and that oleic acid, a dietary fatty acid, directly mediates hyperpermeability of endothelial cells by disrupting adherens junctions. Apelin is required for the assembly of functional vasculature during angiogenesis (11). Interestingly, apelin inhibited oleic acid–induced vascular hyperpermeability by modulating VE-cadherin in vitro. Taken together, these results indicate that HFD-fed apelin KO mice develop abnormal vascular leakiness and structure as a result of the synergistic effects of apelin depletion and increase of oleic acid. Importantly, lymphatic backflush and abnormal leakiness were found in the ear skin of HFD-fed apelin KO mice. In vitro, lymphatic permeability was induced in the presence of fatty acids, whereas apelin attenuated the fatty acid–induced hyperpermeability. Because leakiness and structural abnormalities of skin lymphatic vessels are seen in apolipoprotein E–deficient mice (21), these results suggest that abnormal transportation and lymphatic absorbance of fatty acids from peripheral tissues like skin could be involved in the development of obesity. Moreover, lymphatic hyperplasia was found in the subcutaneous fat layer from extremely obese apelin KO mice in contrast to normal and obese WT mice. In inflamed skin, increased interstitial fluid pressure caused by increased leakage from blood vessels may increase fluid drainage through lymphatic vessels, but this may impair lymphatic function (22). Thus, an increase of lymphatic vessels could facilitate lymphatic drainage and resolution of the related inflammation (23,24). Therefore lymphangiogenesis in adipose tissue could be a significant therapeutic target, although further study is needed to determine whether infiltrated macrophages in obese adipose tissue or mature adipocyte-derived VEGF-C are involved in the promotion of lymphangiogenesis in adipose tissue.

What is the role of apelin in obesity? In vivo, an orally administered COX2 inhibitor rescued apelin KO mice from HFD-induced obesity. A COX2 inhibitor directly affects vascular function, suppressing angiogenesis and lymphangiogenesis associated with tumor growth (19). The COX2 inhibitor, CEL, blocked angiogenesis and blood/lymphatic vessel enlargement in HFD-fed apelin KO mice. In vitro, we found that CEL treatment blocked oleic acid–induced hyperpermeability of lymphatic and blood vessel endothelial cells. Taken together with the fact that several

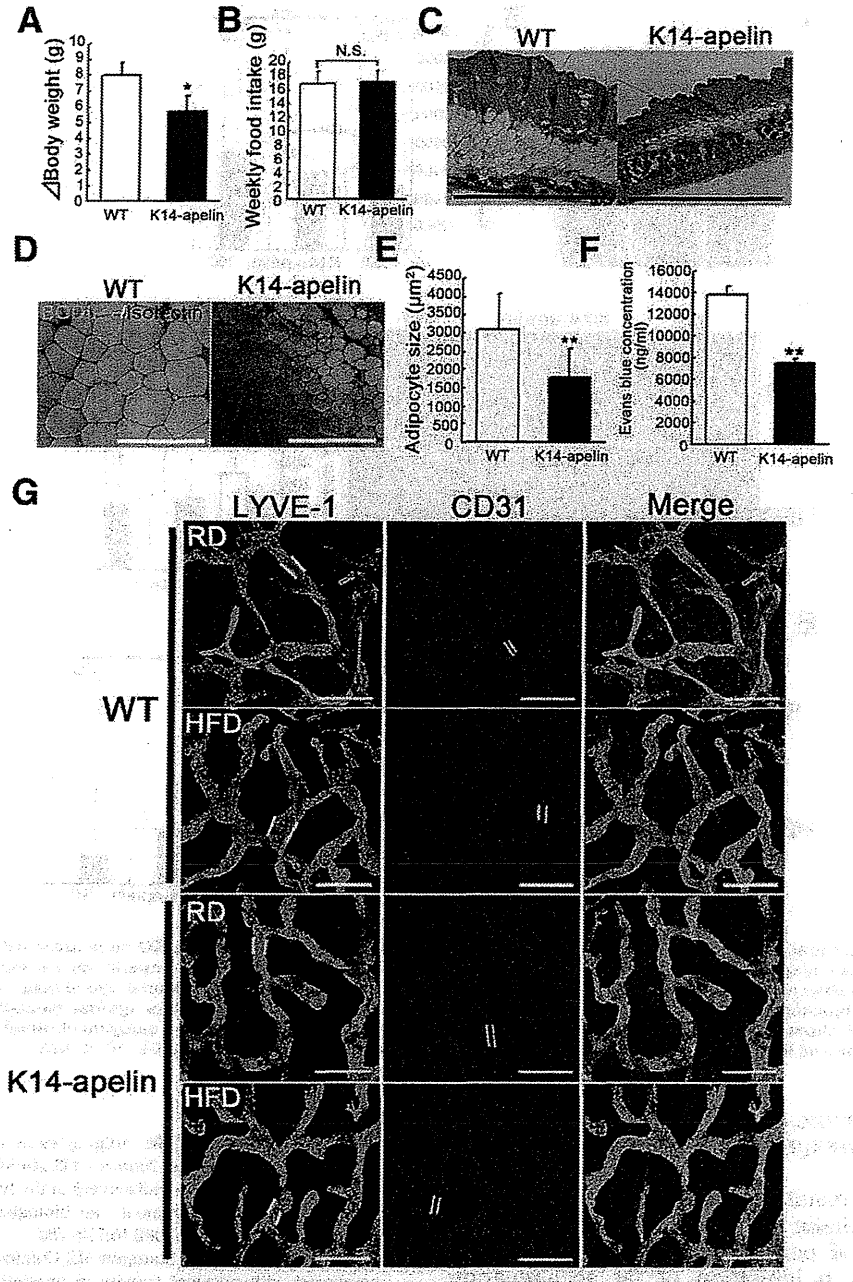

FIG. 6. Resistance to obesity in K14-apelin mice. *A*: Change in body weight of HFD-fed K14-apelin and WT mice ($N = 4–7$). *B*: Average weekly food intake of each genotype. *C*: Hematoxylin and eosin staining of skin sections from HFD-fed, K14-apelin, and WT mice. A reduced subcutaneous adipose layer was found in K14-apelin mice. *D*: BODIPY (green) and Isolectin (red) staining revealed decreased size of subcutaneous adipocytes (green) in K14-apelin mice after HFD feeding. *E*: Morphometric analysis of adipocyte size confirmed that adipocytes were smaller in HFD-fed K14-apelin mice. Data are expressed as mean values ± SD. *F*: Inhibition of lymphatic dye leakage in mesenteric fat of K14-apelin mice after HFD. *G*: Whole-mount staining of mouse ears using antibodies against LYVE-1 (green) and CD31 (red) revealed that HFD induced enlargement of both lymphatic and blood vessels, whereas no significant difference was found between RD- and HFD-fed K14-apelin mice. Two parallel yellow lines as indicated in (*G*) show vascular size. Bars indicate 1 mm (*C*) and 200 μm (*D*, *G*). $^{**}P < 0.01$, $^{*}P < 0.05$.

dietary fatty acids increased the expression level of transcription factors associated with adipocyte differentiation, including peroxisome proliferator–activated receptors (25), leakage of dietary fatty acids, possibly from hyperpermeable vessels, could accelerate adipocyte differentiation. In addition, a selective COX2 inhibitor did not affect fat accumulation of WT mice, although the number of blood vessels in skin was decreased. Taking into account the fact that no significant change of COX2 expression was found after apelin treatment in endothelial cells, this is consistent with the idea that a selective COX2 inhibitor could directly block the development of vascular hyperpermeability in HFD-fed apelin KO mice, leading to inhibition of obesity. The increased leakage of fatty acids attributable to the disruption of lymphatic and vascular function could trigger adipocyte hypertrophy. Recently, it has been reported that overexpression of COX2 in skin increased energy expenditure via recruitment of brown

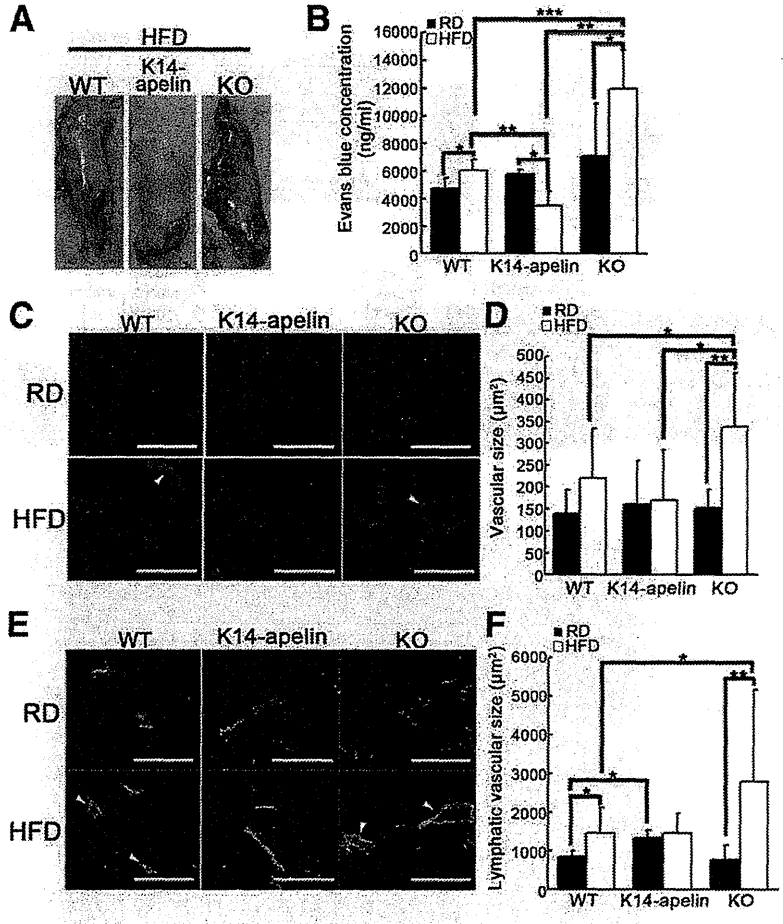

FIG. 7. Structural and functional changes of vessels in the adipose tissues of K14-apelin and apelin KO mice after HFD. *A*: Miles assay revealed increased Evans blue leakage in epididymal fat of apelin KO mice and decreased leakage in that of K14-apelin mice as compared with WT mice after feeding of HFD. *B*: Quantitative analysis of dye leakage in the epididymal fat showed that HFD enhanced dye leakage in WT and apelin KO mice, whereas dye leakage was blocked in K14-apelin mice. Immunofluorescence analysis using antibodies against meca-32 (*C*) and LYVE-1 (*E*) in mesenteric fat. Arrowheads show enlarged blood vessels (*C*) and lymphatic vessels (*E*). Quantitative analysis of blood vessels (*D*) and lymphatic vessels (*F*) in mesenteric fat of WT, K14-apelin, and apelin KO mice. Bars indicate 200 μm. $^{**}P < 0.01$, $^{*}P < 0.05$.

adipocytes (26). Therefore, further investigation of the role of apelin in COX2-overexpressing brown adipose tissue is needed.

In conclusion, our results indicate that apelin/APJ signaling promotes lymphatic and blood vessel integrity and blocks the increase of permeability induced by dietary fatty acids, resulting in inhibition of fat accumulation. Apelin might be a novel target for prevention of obesity and obesity-related diseases via enhancement of vascular integrity.

ACKNOWLEDGMENTS

No potential conflicts of interest relevant to this article were reported.

M.S. and K.K. designed and performed research, analyzed data, and wrote the paper. H.K., M.T., and F.M. performed research and analyzed data. N.T. designed research and wrote the paper. K.K. is the guarantor of this work and, as such, had full access to all the data and takes full responsibility for the integrity of data and accuracy of data analysis.

The authors thank Fumika Miyohashi and Kyo Suin (Shiseido Innovative Science Research Center, Yokohama, Japan) for their technical assistance.

REFERENCES

1. Rosen ED, Spiegelman BM. Adipocytes as regulators of energy balance and glucose homeostasis. Nature 2006;444:847–853
2. Oliver G, Detmar M. The rediscovery of the lymphatic system: old and new insights into the development and biological function of the lymphatic vasculature. Genes Dev 2002;16:773–783
3. Hu FB, Willett WC, Li T, Stampfer MJ, Colditz GA, Manson JE. Adiposity as compared with physical activity in predicting mortality among women. N Engl J Med 2004;351:2694–2703
4. Crandall DL, Hausman GJ, Kral JG. A review of the microcirculation of adipose tissue: anatomic, metabolic, and angiogenic perspectives. Microcirculation 1997;4:211–232
5. Cao Y. Adipose tissue angiogenesis as a therapeutic target for obesity and metabolic diseases. Nat Rev Drug Discov 2010;9:107–115
6. Karkkainen MJ, Saaristo A, Jussila L, et al. A model for gene therapy of human hereditary lymphedema. Proc Natl Acad Sci USA 2001;98:12677–12682
7. Harvey NL, Srinivasan RS, Dillard ME, et al. Lymphatic vascular defects promoted by Prox1 haploinsufficiency cause adult-onset obesity. Nat Genet 2005;37:1072–1081
8. Tatemoto K, Hosoya M, Habata Y, et al. Isolation and characterization of a novel endogenous peptide ligand for the human APJ receptor. Biochem Biophys Res Commun 1998;251:471–476
9. Chen MM, Ashley EA, Deng DX, et al. Novel role for the potent endogenous inotrope apelin in human cardiac dysfunction. Circulation 2003;108:1432–1439
10. Kidoya H, Ueno M, Yamada Y, et al. Spatial and temporal role of the apelin/APJ system in the caliber size regulation of blood vessels during angiogenesis. EMBO J 2008;27:522–534

11. Kidoya H, Naito H, Takakura N. Apelin induces enlarged and nonleaky blood vessels for functional recovery from ischemia. Blood 2010;115:3166–3174
12. Sawane M, Kidoya H, Muramatsu F, Takakura N, Kajiya K. Apelin attenuates UVB-induced edema and inflammation by promoting vessel function. Am J Pathol 2011;179:2691–2697
13. Kajiya K, Hirakawa S, Ma B, Drinnenberg I, Detmar M. Hepatocyte growth factor promotes lymphatic vessel formation and function. EMBO J 2005;24:2885–2895
14. Nishimura S, Manabe I, Nagasaki M, et al. In vivo imaging in mice reveals local cell dynamics and inflammation in obese adipose tissue. J Clin Invest 2008;118:710–721
15. Hirakawa S, Hong YK, Harvey N, et al. Identification of vascular lineage-specific genes by transcriptional profiling of isolated blood vascular and lymphatic endothelial cells. Am J Pathol 2003;162:575–586
16. Yamamoto Y, Yoshimasa Y, Koh M, et al. Constitutively active mitogen-activated protein kinase kinase increases GLUT1 expression and recruits both GLUT1 and GLUT4 at the cell surface in 3T3-L1 adipocytes. Diabetes 2000;49:332–339
17. Calkhoven CF, Müller C, Leutz A. Translational control of C/EBPalpha and C/EBPbeta isoform expression. Genes Dev 2000;14:1920–1932
18. Reaux A, De Mota N, Skultetyova I, et al. Physiological role of a novel neuropeptide, apelin, and its receptor in the rat brain. J Neurochem 2001;77:1085–1096
19. Iwata C, Kano MR, Komuro A, et al. Inhibition of cyclooxygenase-2 suppresses lymph node metastasis via reduction of lymphangiogenesis. Cancer Res 2007;67:10181–10189
20. Mäkinen T, Jussila L, Veikkola T, et al. Inhibition of lymphangiogenesis with resulting lymphedema in transgenic mice expressing soluble VEGF receptor-3. Nat Med 2001;7:199–205
21. Lim HY, Rutkowski JM, Helft J, et al. Hypercholesterolemic mice exhibit lymphatic vessel dysfunction and degeneration. Am J Pathol 2009;175:1328–1337
22. Kajiya K, Hirakawa S, Detmar M. Vascular endothelial growth factor-A mediates ultraviolet B-induced impairment of lymphatic vessel function. Am J Pathol 2006;169:1496–1503
23. Huggenberger R, Ullmann S, Proulx ST, Pytowski B, Alitalo K, Detmar M. Stimulation of lymphangiogenesis via VEGFR-3 inhibits chronic skin inflammation. J Exp Med 2010;207:2255–2269
24. Kajiya K, Sawane M, Huggenberger R, Detmar M. Activation of the VEGFR-3 pathway by VEGF-C attenuates UVB-induced edema formation and skin inflammation by promoting lymphangiogenesis. J Invest Dermatol 2009;129:1292–1298
25. Madsen L, Petersen RK, Kristiansen K. Regulation of adipocyte differentiation and function by polyunsaturated fatty acids. Biochim Biophys Acta 2005;1740:266–286
26. Vegiopoulos A, Müller-Decker K, Strzoda D, et al. Cyclooxygenase-2 controls energy homeostasis in mice by de novo recruitment of brown adipocytes. Science 2010;328:1158–1161

THE JOURNAL OF BIOLOGICAL CHEMISTRY VOL. 288, NO. 18, pp. 12469–12477, May 3, 2013

Ligand-independent Tie2 Dimers Mediate Kinase Activity Stimulated by High Dose Angiopoietin-1*[S]

Received for publication, November 5, 2012, and in revised form, February 19, 2013 Published, JBC Papers in Press, March 15, 2013, DOI 10.1074/jbc.M112.433979

Daishi Yamakawa[‡], Hiroyasu Kidoya[‡], Susumu Sakimoto[‡], Weizhen Jia[‡], Hisamichi Naito[‡], and Nobuyuki Takakura[‡§1]

From the [‡]Department of Signal Transduction, Research Institute for Microbial Diseases, Osaka University, 3-1 Yamada-oka, Suita-shi, Osaka 565-0871, Japan and [§]Japan Science and Technology Agency (JST), Sanbancho, Chiyoda-ku, Tokyo 102-0075, Japan

Background: Tie2 is essential for angiogenesis and vascular stabilization.
Results: Tie2, but not Tie1, forms ligand-independent dimers on the cell surface.
Conclusion: The inactive monomer mutant Tie2YIA/LAS decreases Ang1/Tie2 signaling.
Significance: The Tie2 ligand-independent dimer induces strong phosphorylation upon high dose Ang1 binding.

Tie2 is a receptor tyrosine kinase expressed on vascular endothelial cells (ECs). It has dual roles in promoting angiogenesis and stabilizing blood vessels, and it has been suggested that Tie2 forms dimers and/or oligomers in the absence of angiopoietin-1 (Ang1); however, the mechanism of ligand-independent dimerization of Tie2 and its biological significance have not been clarified. Using a bimolecular fluorescence complementation assay and a kinase-inactive Tie2 mutant, we show here that ligand-independent Tie2 dimerization is induced without Tie2 phosphorylation. Moreover, based on the fact that Tie1 never forms heterodimers with Tie2 in the absence of Ang1 despite having high amino acid sequence homology with Tie2, we searched for ligand-independent dimerization domains of Tie2 by reference to the difference with Tie1. We found that the YIA sequence of the intracellular domain of Tie2 corresponding to the LAS sequence in Tie1 is essential for this dimerization. When the YIA sequence was replaced by LAS in Tie2 (Tie2YIA/LAS), ligand-independent dimer was not formed in the absence of Ang1. When activation of Tie2YIA/LAS was induced by a high dose of Ang1, phosphorylation of Tie2 was limited compared with wild-type Tie2, resulting in retardation of activation of Erk downstream of Tie2. Therefore, these data suggest that ligand-independent dimerization of Tie2 is essential for a strong response upon stimulation with high dose Ang1.

The functions of angiopoietin-1 (Ang1),[2] a ligand for receptor tyrosine kinase Tie2 expressed on endothelial cells (ECs), in both EC-to-EC and EC-to-mural cell adhesion are well established (1–4). Although Ang1-Tie2 signaling is involved in promoting maturation and quiescence of blood vessels mainly regulated by Akt signal transduction via the p85 subunit of PI3K, Tie2 also has proangiogenic activity mediated by MAPK signaling (5–7). Because Tie2 possesses both anti-angiogenic as well as proangiogenic properties, it is important to investigate how Tie2 activation is altered during angiogenesis. The Tie receptor family consists of Tie2 and Tie1 (8–10). Recent studies show that Ang1 activates Tie1 indirectly by interactions with Tie2 (11). When Tie1 expression is silenced, Tie2 signaling especially via the MAPK pathway is enhanced; accordingly, Tie1-deficient mice show hyperproliferative vascular formation and vascular abnormalities (12, 13). This suggests that Tie1 may negatively regulate angiogenic signaling by Tie2.

Tie2 is composed of an extracellular domain, one transmembrane domain, and an intracellular tyrosine kinase domain split into two by a non-kinase sequence. Tie1 has high amino acid sequence homology with Tie2 (76 and 33% identity in intracellular and extracellular domains, respectively). Based on the isolation of Tie2 ligands and analysis of signal transduction through Tie2, it is widely accepted that Ang1 activates Tie2, but Ang2 binding inhibits its signaling. Thus, with certain exceptions Ang2 acts as an Ang1 antagonist (4, 13–18).

It is known that Tie2 is present on the EC surface in the form of dimers and higher order oligomers, as established by electron microscopy (19). It has been reported that EGF receptor, erythropoietin receptor, and TNF receptor also dimerize in a ligand-independent manner (20–25). Ligand-independent dimerization of EGF receptor does not lead to tyrosine phosphorylation of EGF receptor. It has been suggested that a conformational change of the EGF receptor induces kinase activity on ligand binding. Therefore, ligand-independent dimers may mediate rapid signal transduction responses. Although Tie2 also forms ligand-independent dimers, the importance of this has not yet been determined.

In the present study, we established a system for visualization of Tie2 dimers using bimolecular fluorescence complementation (BiFC) assays in living cells (26). Using this system, we sought Ang1-independent Tie2-Tie2 dimerization domains. We generated a Tie2 mutant that does not form dimers in the absence of Ang1. We investigated the biological significance of ligand-independent Tie2 dimerization using this mutant.

* This work was supported in part by a grant from the Ministry of Education, Science, Sports, and Culture of Japan.
[S] This article contains supplemental Table S1 and Figs. S1–S6.
[1] To whom correspondence should be addressed: Dept. of Signal Transduction, Research Institute for Microbial Diseases, Osaka University, 3-1 Yamada-oka, Suita-shi, Osaka 565-0871, Japan. Tel.: 81-6879-8316; Fax: 81-6879-8314; E-mail: ntakaku@biken.osaka-u.ac.jp.
[2] The abbreviations used are: Ang1, angiopoietin-1; EC, endothelial cell; BiFC, bimolecular fluorescence complementation; Ab, antibody.

EXPERIMENTAL PROCEDURES

Reagents and Antibodies—Recombinant human Angl was purchased from R&D Systems. In Western blot analysis, mouse anti-phosphotyrosine (4G10) and anti-Tie2 (Ab33) antibodies (Abs) (Upstate), anti-HA.11 mAb (COVANCE), anti-c-Myc (9E10) and Tie1 (C-18) mAbs (Santa Cruz Biotechnology, Inc.), anti-HA-tag rabbit serum (Medical & Biological Laboratories Co., Ltd.), p44/42, phospho-p44/42 (Thr^{202}/Tyr^{204}), phospho-Tie2 (Tyr^{992}) Abs (Cell Signaling Technology, Inc.) and mouse anti-HA (12CA5) mAb (Roche Diagnostics) were used as the first Abs. Anti-phospho-Tie2 (Tyr^{992}) and anti-phosphotyrosine Abs were diluted 1:500, and others were diluted 1:1000. HRP-conjugated anti-rabbit and anti-mouse IgG (Jackson ImmunoResearch Laboratories) was used as the secondary antibody (dilution: 1:1000). For the immunofluorescence analysis, HA and Myc were used as the first Abs (dilution, 1:100). Alexa Fluor 546-conjugated goat anti-rabbit Igs and Alexa Fluor 647-conjugated goat anti-mouse Igs were used as the secondary Abs (Invitrogen) (dilution, 1:200).

Plasmid Construction—Mouse Tie2 and Tie1 were fused to sequences encoding full-length Venus and Venus residues 1–173 amino acids (VN) or 155–238 amino acids (VC). The coding regions were connected with linker sequences encoding RSAIT (Arg-Ser-Ala-Ile-Thr). RSAIT is a non-adhesion sequence (26). HA or Myc epitopes were inserted as tags between linker and fluorescent genes. Genes were inserted at the multicloning site in pEGFPN1 vector or pMRX virus vector. Basing the work on the pE-Tie2-linker-Myc-Venus, pE-Tie2-linker-HA-VN and pE-Tie2-linker-Myc-VC, we cut between the BamHI and MluI sites and the Tie2 mutant (Tie2K854R, Tie2R848W) was created. Tie2 kinase-dead (Tie2K854R) or Tie2 constitutive-active (Tie2R848W) mutants were amplified from wild-type Tie2 using Tie2K854R-N, -C primers or Tie2R848W-N, -C primers, respectively (supplemental Table S1).

For the generation of Tie1*, the signal sequence of Tie2 was amplified from the Tie2 plasmid using oligonucleotide primers (forward primer, 5′-GTA GGC GTG TAC GGT GGG AGG TCT-3′ and reverse primer, 5′-GTT AAG TCA ACA GAG CCT TCT ACT ACT CC-3′) and 5′-Tie1 core sequence excluding signal sequence was amplified from Tie1 using oligonucleotide primers (forward primer, 5′-GGA GTA GTA GAA GGC TCT GTT GAC TTA AC-3′ and reverse primer, 5′-CCA CTT CTG AGC TTC ACA GCC TCG CAC GAT-3′). These two products were amplified with the forward primer for Tie2 and the reverse primer for Tie1. This PCR product was placed into EcoRI and AgeI sites of the Tie1 plasmid. For the generation of Tie2/Tie1 chimeric plasmids, mutagenesis was performed on Tie2 and Tie1 plasmids as templates by using specific primer sets (supplemental Table S1). For generation of 1–3 amino acid mutants of each Tie2 plasmid, mutagenesis was performed using specific primers (supplemental Table S1).

Retroviral Infection—Plat-E cells were transfected with pMRX-Tie2-linker-Myc-Venus, pMRX-Tie2YIA/LAS-linker-Myc-Venus, pMRX-Tie2-linker-HA-VN173 and pMRX-Tie2-linker-Myc-VC155, pMRX-Tie2YIA/LAS-linker-HA-VN173 and pMRX-Tie2YIA/LAS-linker-Myc-VC155 vectors as indicated in each experiment (1.0 μg each) using Lipofectamine 2000 (Invitrogen) and then incubated for 24 h at 37 °C after which the medium was changed. After 12 (36 h from transfection) and 24 h (48 h from transfection), conditioned medium was harvested, sterilized by filtration, and used to infect NIH3T3 cells. 8 μg/ml polybrene was added for enhancement of infection. Stable cell lines were selected by culture in medium containing puromycin (5 μg/ml) or blasticidin (10 μg/ml) (27, 28).

Cell Culture—HEK293T and NIH3T3 lines were grown in DMEM supplemented with 10% FBS. Platinum-E cells (Plat-E; packaging cells) and stable cell lines transfected by pMRX virus vector were cultured in 10% FBS containing DMEM.

Transfection and Bimolecular Fluorescence Complementation Analysis—To carry out BiFC in living cells, cells were co-transfected with the expression vectors indicated in each experiment (1.0 μg each) using Lipofectamine 2000. The fluorescence emissions were acquired in living cells 22–48 h after transfection using a fluorescence microscope with a cooled CCD camera, or by flow cytometry. Protein expression levels were assessed by Western blotting.

Cell Lysis, Immunoprecipitation, SDS-PAGE, and Western Blotting—Cells were washed with ice-cold PBS and lysed with radioimmune precipitation assay lysis buffer (50 mM Tris-HCl, pH 7.5, 150 mM NaCl, 1% Nonidet P-40, 0.5% sodium deoxycholate, 0.1% SDS). The cells were incubated on ice for 10 min followed by centrifugation at 15,000 rpm for 5 min at 4 °C. Cells were immunoprecipitated from the supernatant using 1–2 μg of anti-Myc Ab that had been precoupled to 20 μl of protein A-Sepharose 4 Fast Flow (GE Healthcare).

Proteins electrophoretically separated using 7.5% SDS gels were transferred to nylon membranes (Amersham Biosciences) by a wet blotting procedure (140 V, 200 mA, 120 min). The membrane was blocked with 5% skim milk/TBST for 60 min, subsequently incubated with the Abs as indicated in the figures and processed for chemiluminescence detection with ECL solution. Densitometry was performed with NIH ImageJ software (version 1.43u).

FACS Analysis—BiFC was analyzed by flow cytometry. After fluorescence complementation, cells were washed with PBS and resuspended in PBS. FACS analysis was performed with a FACSCalibur (BD Biosciences) using the 488 nm laser for excitation and a 515–545 nm band pass filter for detection. For quantitative evaluation of BiFC fluorescence, we used % Gated (fluorescent cells) × *X* Geo Mean (average of fluorescent intensity) as arbitrary fluorescence units.

Confocal Laser Scanning Microscopy—Transfected cells on 0.1% gelatin-coated glass dishes (Sigma Aldrich) were rinsed, fixed for 10 min in 4% paraformaldehyde-PBS (pH 7.5), and washed with PBS. Subsequently, the cells were permeabilized with 0.1% Triton X-100 for 10 min. After washing with PBS, cells were blocked with PBS containing 5% normal goat serum and 1% BSA for 30 min and immunostained with first Ab (1:100) for 1 h. Protein reacting with Ab was visualized with secondary Abs (1:200). HA or Myc epitopes were inserted as tags between Tie2 or Tie2YIA/LAS and the BiFC tag (VN or VC). HA-VN fused with Tie2 or Tie2YIA/LAS was stained by rabbit anti-HA Ab (Medical & Biological Laboratories Co., Ltd.) and Alexa Fluor 546 (red)-conjugated anti-rabbit Igs. Myc-VC fused with Tie2 or Tie2YIA/LAS was stained with